

The EUMETSAT Satellite Application Facility on Land Surface Analysis (LSA SAF)

Validation Report Normalized Difference Vegetation Index (ENDVI10) LSA-420



Reference Number:
Issue/Revision Index:
Last Change:

SAF/LAND/VR_ENDVI10v2/1.0
Issue 1
12/11/2019

DOCUMENT SIGNATURE TABLE

	Name	Date	Signature
Prepared by:	C. Toté, E. Swinnen, E. Wolters, B. Smets	12/11/2019	
Approved by:	LSA SAF Project Manager		

DOCUMENTATION CHANGE RECORD

Issue / Revision	Date	Description :
Issue 0	21/09/2018	Version for ORR
Issue 1	12/11/2019	Version for ORR

TABLE OF CONTENTS

TABLE OF CONTENTS	3
LIST OF TABLES	5
LIST OF FIGURES	5
LIST OF ACRONYMS	7
1 INTRODUCTION.....	9
1.1 Land Surface Analysis – Satellite Application Facility	9
1.2 The EUMETSAT Polar System	9
1.3 The ENDVI10 version 1 product (ENDVI10 v1)	9
1.4 The ENDVI10 version 2 product (ENDVI10 v2)	10
1.5 Objectives	10
1.6 Related documents.....	11
2 VALIDATION METHODS.....	12
2.1 Overall procedure.....	12
2.2 Validation metrics.....	13
2.2.1 Coefficient of determination (R^2).....	13
2.2.2 Geometric mean regression	13
2.2.3 The root mean squared difference (RMSD).....	14
2.2.4 Random and systematic differences (RMPDu and RMPDs).....	14
2.2.5 Mean Bias Error (MBE).....	14
2.3 Sampling	14
2.4 Geometric accuracy	17
2.5 Satellite reference products	19
2.5.1 LSA SAF – ENDVI10 version 1 based on MetOp/AVHRR (ENDVI10 v1).....	19
2.5.2 Copernicus GLS – NDVI v2.2 based on PROBA-V (CGLS NDVI v2.2)	19
2.6 Regional/Biome assessment.....	19
2.6.1 Stratification per biome.....	19
2.6.2 BELMANIP2 and DIRECT sites	20
2.6.3 Latitude bands.....	21
3 VALIDATION OF ENDVI10 V2	22
3.1 Product completeness.....	22
3.1.1 Temporal evolution of product completeness.....	22
3.1.2 Spatial distribution of product completeness.....	23
3.1.3 Gap length frequency.....	24
3.2 Spatial consistency	25
3.2.1 Histograms per biome	25
3.2.2 Spatial distribution of validation metrics	27
3.3 Statistical consistency.....	30
3.3.1 ENDVI10 v2 vs. ENDVI10 v1.....	30
3.3.2 Comparison with CGLS NDVI v2.2.....	34
3.4 Temporal consistency.....	36
3.4.1 Temporal smoothness	36
3.4.2 Temporal variations and realism.....	37
4 CONSISTENCY BETWEEN SENSORS	44
4.1 Radiometry (ENDVI10).....	44
4.1.1 MetOp-A vs. MetOp-B (2016).....	44
4.1.2 MetOp-B vs. MetOp-C (2019).....	45
4.1.3 MetOp-A, -B, -C vs. CGLS NDVI v2.2	46

4.2 Geometric accuracy	47
5 SUMMARY AND CONCLUSIONS.....	51
REFERENCES	53
ANNEX 1.....	54
ANNEX 2.....	56
ANNEX 3.....	57

List of Tables

Table 1. Product Requirements for ENDVI10, in terms of area coverage, resolution, and accuracy. R^2 denotes the coefficient of determination (explained variance) between paired (same day and cloud/snow-free) observations of MetOp-AVHRR and SPOT-VGT / PROBA-V. When this is not possible, R^2 is estimated from matches of 10-day composites with the respective ENDVI10 10-day synthesis.....	11
Table 2. Overall procedure for the quality assessment of ENDVI10 v2.	12
Table 3. Aggregation scheme for GLC2000 classes into 7 major biomes and proportion of each biome at global scale.	20
Table 4. PROBA-V and MetOp-B/AVHRR flight characteristics, equatorial overpass times, and RED and NIR spectral ranges (Full Width at Half Maximum, FWHM).	55

List of Figures

Figure 1. Temporal evolution over 2016 – 2018 of the global number of observations [%] retained after additional sampling for the ‘ViewAngle’, ‘IllumAngle’ and ‘ViewAngle+IllumAngle’ sampling schemes for the Intercomparison between ENDVI10 v2 and ENDVI10 v1.....	15
Figure 2. Spatial distribution of the number of observations (%) retained after additional sampling for the ‘ViewAngle’, ‘IllumAngle’ and ‘ViewAngle+IllumAngle’ sampling schemes over 2016 – 2018 for the Intercomparison between ENDVI10 v2 and ENDVI10 v1.....	16
Figure 3. Temporal evolution over January-December 2016 of the global number of observations [%] retained after additional sampling for the ‘ViewAngle’ sampling scheme for the Intercomparison between ENDVI10 v2 based on MetOp-A and MetOp-B.	16
Figure 4. Spatial distribution of the number of observations (%) retained after additional sampling for the ‘ViewAngle’ sampling schemes over January-December 2016 for the Intercomparison between ENDVI10 v2 based on MetOp-A and MetOp-B.....	17
Figure 5. Temporal evolution over July-September 2019 of the global number of observations [%] retained after additional sampling for the ‘ViewAngle’ sampling scheme for the intercomparison between ENDVI10 v2 based on MetOp-B and MetOp-C.	17
Figure 6. Spatial distribution of the number of observations (%) retained after additional sampling for the ‘ViewAngle’ sampling scheme over July-September 2019 for the Intercomparison between ENDVI10 v2 based on MetOp-B and MetOp-C.	17
Figure 7. The GLC classification aggregated into 7 classes.	19
Figure 8. Spatial distribution of the BELMANIP2 (blue) and DIRECT (pink) sites.	21
Figure 9. Latitude bands used for spatio-temporal analysis (left) and number of pixels per band (right)....	21
Figure 10. Temporal evolution of the amount of good observations over 2016 – 2018 at global scale for ENDVI10 v2 (blue), ENDVI10 v1 (green) and CGLS NDVI v2.2 (red).....	23
Figure 11. Spatial distribution of missing values occurrence frequency (%) over 2016 – 2018 for ENDVI10 v2 (top), ENDVI10 v1 (middle) and CGLS NDVI v2.2 (bottom).....	24
Figure 12. Difference in spatial distribution of missing values occurrence frequency between ENDVI10 v2 and ENDVI10 v1 (%) over 2016 – 2018.....	24
Figure 13. Frequency distribution of the gap length (in dekads) over 2016 – 2018 at global scale for ENDVI10 v2 (blue), ENDVI10 v1 (green) and CGLS NDVI v2.2 (red).....	25
Figure 14. Frequency distributions over 7 different biomes. Pairwise comparison of physical NDVI values for ENDVI10 v2 (green), ENDVI10 v1 (red) and CGLS NDVI v2.2 (blue) over 2016-2018. X-axis: NDVI values with bin sizes of 0.1, Y-axis: occurrence frequency [%].	26
Figure 15. RMSD, RMPDs and RMPDu between ENDVI10 v2 and ENDVI10 v1 for MetOp-B, 2016 – 2018. .	27
Figure 16. RMSD, RMPDs, and RMPDu between MetOp-B ENDVI10 v2 (left) and ENDVI10 v1 (right) and CGLS NDVI v2.2 for 2016 – 2018.	29
Figure 17. Scatterplots between ENDVI10 v2 (X) and ENDVI10 v1 (Y) over all land cover types (top left) and per biome at global scale. The dashed lines indicate the 1:1 relation, while the red solid lines denote the GM regression. Note the logarithmic color scale of the bin densities.....	31

Figure 18. Scatterplots between ENDVI10 v2 (X) and ENDVI10 v1 (Y) over all land cover types (top left) and per biome at global scale, using the 'ViewAngle' sampling scheme.....	32
Figure 19. Scatterplots between ENDVI10 v2 (X) and ENDVI10 v1 (Y) over all land cover types (top left) and per biome at global scale, using the 'IllumAngle' sampling scheme.....	33
Figure 20. Scatterplots between ENDVI10 v2 (X) and ENDVI10 v1 (Y) over all land cover types (top left) and per biome at global scale, using the 'ViewAngle+IllumAngle' sampling scheme.....	34
Figure 21. Scatterplots between ENDVI10 v2 (X) and CGLS NDVI v2.2 (Y) over all land cover types (top left) and per biome at global scale.....	35
Figure 22. Scatterplots between ENDVI10 v1 (X) and CGLS NDVI v2.2 (Y) over all land cover types (top left) and per biome at global scale.....	36
Figure 23. Intercomparison of δ frequency histograms, a measure for temporal smoothness.....	37
Figure 24. Temporal profiles of ENDVI10 v2, ENDVI10 v1 and CGLS NDVI v2.2 over a number of BELMANIP2 and DIRECT sites.....	43
Figure 25. Scatterplots between MetOp-B ENDVI10 v2 (X) and MetOp-A ENDVI10 v2 (Y) over all biome types. Analysis without additional sampling (left) and with additional 'ViewAngle' sampling (right).....	44
Figure 26. Histograms of the bias between MetOp-B ENDVI10 v2 and MetOp-A ENDVI10 v2 over all land cover types. Analysis without additional sampling (left) and with additional 'ViewAngle' sampling (right).	45
Figure 27. Histograms of the VZA of paired observations between MetOp-B ENDVI10 v2 and MetOp-A ENDVI10 v2 over all land cover types. Analysis without additional sampling (left) and with additional 'ViewAngle' sampling (right).....	45
Figure 28. Scatterplots between MetOp-B ENDVI10 v2 (X) and MetOp-C ENDVI10 v2 (Y) over all biome types. Analysis without additional sampling (left) and with additional 'ViewAngle' sampling (right).....	46
Figure 29. Histograms of the bias between MetOp-B ENDVI10 v2 (X) and MetOp-C ENDVI10 v2 (Y) over all land cover types. Analysis without additional sampling (top left) and with additional 'ViewAngle' sampling (right).	46
Figure 30. Histograms of the VZA of paired observations between MetOp-B ENDVI10 v2 and MetOp-A ENDVI10 v2 over all land cover types. Analysis without additional sampling (left) and with additional 'ViewAngle' sampling (right).....	46
Figure 31. Hovmöller plots showing the spatio-temporal distribution of RMSD, RMPDs, RMPDu and MBE between a test dataset of ENDVI10 v2 combining MetOp-A, -B, and -C with CGLS NDVI v2.2 for January 2016 – September 2019.	47
Figure 32. Geolocation accuracy for MetOp-A – C, 2016 – 2019, for (upper panel) aggregated longitudinal (dx) and latitudinal (dy) deviations, (middle panel) dx deviations, and (bottom panel) dy deviations.	49
Figure 33. Geolocation S10 accuracy values for 20160401 for MetOp-A (left column) and MetOp-B (right column). The upper row shows the aggregated dx and dy geolocation accuracy, while the separate dx and dy components (expressed in absolute values) are shown in the middle and bottom row, respectively. Low geolocation deviations are indicated by blue colors and transform towards red for larger deviations.	50
Figure 34. (upper panel) Spectral Response Functions for PROBA-V (solid lines), Terra-MODIS (dotted lines), and MetOp-B-AVHRR (dashed lines). Reference grass, maple leaf, and sandy loam spectra are shown in dark green (solid), dark green (dashed), and dotted brown lines, respectively. (middle panel) RED channel Spectral Response Functions for MetOp-A – C, (bottom panel) NIR channel Spectral Response Functions for MetOp-A – C.	54
Figure 35. Static latitudinal AOT (upper plot) and the difference between CAMS _{CLIM} and static latitudinal AOT for 1 – 10 January (second row, left), 1 – 10 April (second row, right), 1 – 10 July (bottom row, left), and 1 – 10 October (bottom row, right).....	56

List of Acronyms

Acronym	Definition
AERONET	Aerosol Robotic Network
AOT	Aerosol Optical Thickness
ASCAT	Advanced Scatterometer
ATBD	Algorithm Theoretical Basis Document
AVHRR	Advanced Very High Resolution Radiometer
BA	Bare areas
BDF	Broadleaved Deciduous Forests
BEF	Broadleaved Evergreen Forests
BELMANIP	Benchmark Land Multisite Analysis and Intercomparison of Products
BHR	Bi-Hemispherical Reflectance
BRDF	Bidirectional Reflectance Distribution Function
C3S	Copernicus Climate Change Service
CAMS	Copernicus Atmospheric Monitoring Service
CDR	Climate Data Record
CEOS	Committee on Earth Observation Systems
CGLS	Copernicus Global Land Service
CUL	Cultivated areas and cropland
EC	European Commission
ENDVI	EPS Normalized Difference Vegetation Index
EOS	Earth Observing System
EPS	EUMETSAT Polar System
EUMETSAT	European organization for the Exploitation of Meteorological Satellites
EVI	Enhanced Vegetation Index
FWHM	Full Width at Half Maximum
GCP	Ground Control Point
GLC	Global Land Cover
GM	Geometric Mean
GMR	Geometric Mean Regression
HER	Herbaceous cover
ICDR	Interim Climate Data Record
iCOR	Atmospheric Image Correction for Land and Water
JRC	Joint Research Centre
LPV	Land Product Validation
LSA	Land Surface Analysis
LST	Land Surface Temperature
MACC	Monitoring Atmospheric Composition & Climate
MARS	Monitoring Agricultural ResourceS
MBE	Mean Bias Error
MetOp	Meteorological-Operational
MODIS	Moderate Resolution Imaging Spectroradiometer
MPDs	Systematic Mean Product Difference
MPDu	Unsystematic Mean Product Difference
MSD	Mean Squared Difference
MSD	Mean Squared Difference
MSG	Meteosat Second Generation
NASA	National Aeronautics and Space Administration
NDVI	Normalized Difference Vegetation Index
NIR	Near Infrared
NLF	Needleleaved Forests

NOAA	National Oceanic and Atmospheric Administration
NOAA	National Oceanic and Atmospheric Administration
NRT	Near Real Time
PMAp	Polar Multi-Sensor Aerosol Optical Properties
PRD	Product Requirements Document
PROBA-V	PRoject for OnBoard Autonomy - Vegetation
PUM	Product User Manual
RGB	Red Green Blue
RMPDs	Systematic Root Mean Product Difference
RMPDu	Unsystematic Root Mean Product Difference
RMSD	Root Mean Squared Difference
SAF	Satellite Application Facility
SEVIRI	Spinning Enhanced Visible and Infrared Imager
SHR	Shrubland
SMAC	Simplified Model for Atmospheric Correction
SPOT	Satellites Pour l'Observation de la Terre
SWIR	Shortwave Infrared
SZA	Solar Zenith Angle
TOA	Top of Atmosphere
TOC	Top of Canopy
VGT	Vegetation
VR	Validation Report
VZA	Viewing Zenith Angle
WGS84	World Geodetic System 1984

1 Introduction

1.1 Land Surface Analysis – Satellite Application Facility

The Satellite Application Facility (SAF) on Land Surface Analysis (LSA) is part of the SAF Network, a set of specialized development and processing centers, serving as EUMETSAT (European organization for the Exploitation of Meteorological Satellites) distributed Applications Ground Segment. The SAF network complements the product-oriented activities at the EUMETSAT Central Facility in Darmstadt. LSA SAF's main purpose is to take full advantage of remotely sensed data, particularly those available from EUMETSAT sensors, and to measure land surface variables, which will find primarily applications in meteorology (<http://landsaf.ipma.pt/>).

The LSA SAF provides near-real-time and offline products and user support for a wide range of land surface variables related to: (i) surface radiation, both long- and short-wave components; (ii) vegetation, including state, stress and wild fires; and (iii) the energy budget at the surface and mass exchange, combining information on the radiation budget and vegetation state. Given the broad thematic nature of the user community targeted for these products, priority is given to areas related to meteorology, climate and environment, and agriculture applications.

1.2 The EUMETSAT Polar System

The EUMETSAT Polar System (EPS) is Europe's first polar orbiting operational meteorological satellite system and the European contribution to a joint polar system with the USA. EUMETSAT has the operational responsibility for the "morning orbit" with the Meteorological-Operational (MetOp) satellites, the first of which (MetOp-A) was successfully launched on 19 October 2006, the second (MetOp-B) launched on 17 September 2012 and the third MetOp satellite (MetOp-C) launched on 7 November 2018. Despite the wide range of sensors on-board MetOp (<http://www.eumetsat.int/>), most LSA SAF parameters make use of the Advanced Very High Resolution Radiometer (AVHRR) and, to a lesser extent, of the Advanced Scatterometer (ASCAT).

1.3 The ENDVI10 version 1 product (ENDVI10 v1)

The MetOp-AVHRR S10 EPS Normalized Difference Vegetation Index (ENDVI10) data are near-global, 10-daily composite images which are synthesized from the "best available" observations registered per dekad (10-day period) by the orbiting earth observation instrument MetOp-AVHRR. The NDVI is calculated from the AVHRR RED and near-infrared (NIR) atmospherically corrected (i.e. Top of Canopy, TOC) spectral reflectances as follows:

$$NDVI_{TOC} = \frac{(NIR_{TOC} - RED_{TOC})}{(NIR_{TOC} + RED_{TOC})} \quad (\text{Eq. 1})$$

On behalf of the Joint Research Centre – Monitoring Agricultural ResourceS (JRC-MARS) program of the European Commission (EC), VITO developed a NOAA-AVHRR data processing chain over Europe. Individual tracks/orbits are ingested, corrected in different steps (calibration, geometric correction, atmospheric correction, cloud/snow labelling, etc.) and then composited to 10-daily synthesis images (S10). With this chain, all daytime-observed NOAA data registered since 1981 were processed by different research institutes in Europe.

The procedures were adapted for AVHRR/MetOp Level 1b data. The resulting global MetOp-AVHRR S10 composites (ENDVI10) are very comparable with those delivered by VITO's

SPOT-VEGETATION and PROBA-V processing chain: 1 km resolution, near-global daily coverage, a 10-day frequency ("dekad"), and similar spectral characteristics: RED (0.58 - 0.68 μm), Near Infrared (NIR, 0.725 - 1.00 μm), Shortwave Infrared (SWIR, 1.58 - 1.64 μm) - no BLUE, but two Thermal Infrared (TIR) bands. In addition to the basic image layers (surface reflectances, solar and viewing geometry angles, status map, etc.), the dekadal composites also comprise two "value-added" image layers: NDVI and Land Surface Temperature (LST). The ENDVI10 version 1 (v1) product is operated in the LSA SAF System II at VITO.

1.4 The ENDVI10 version 2 product (ENDVI10 v2)

The ENDVI10 version 2 (ENDVI10 v2), which is evaluated in this report, should become available as a Climate Data Record (CDR, LSA-454) starting in March 2007 and as an Intermediate Climate Data Record (ICDR, LSA-420), providing continuous updates in NRT of LSA-454. In both cases, the ENDVI10 consists of NDVI composites and is distributed together with a set of ancillary datasets (surface reflectances, solar and viewing zenith angles, and quality indicators), similar to ENDVI10 v1.

Similar to the previous version (LSA-410 and LSA-453, i.e. ENDVI10 v1) the atmospheric correction is still performed using the Simplified Model for Atmospheric Correction (SMAC) (Rahman and Dedieu, 1994), but rather than using AOT information from a time- and longitude-invariant latitudinal function, more actual and accurate AOT data from the Copernicus Atmospheric Monitoring Service (CAMS) are used.

The CAMS re-analysis (hereafter referred to as CAMS_{CLIM}) is the latest global re-analysis dataset of atmospheric composition (AC) produced by CAMS, assimilating an extensive suite of atmospheric components satellite retrievals. For AOT, retrievals from Moderate Resolution Imaging Spectroradiometer (MODIS)-Aqua and -Terra, and Environmental Satellite (ENVISAT) Advanced Along-Track Scanning Radiometer (AATSR) are assimilated. More scientific and technical details on CAMS re-analysis data can be found in Inness et al. (2019).

Although SMAC is a fast atmospheric correction algorithm, it has considerable limitations in situations with moderate to high aerosol and water vapor loads, as well as for high solar and viewing zenith angles. Therefore, in order to find a trade-off between having a certain extent of spatio-temporal AOT variation and respecting the SMAC limitations, a choice was made to generate a 10-daily AOT climatology based on the 30th percentile of the CAMS re-analysis data for 2003 – 2017. In addition, SMAC calculations over a range of VZA, SZA, RED TOA, and AOT were performed to further constrain the AOT input for SMAC. See the ENDVI10 v2 ATBD for more details on the climatology calculation methodology, as well as on the additional AOT constraints applied.

1.5 Objectives

This Validation Report (VR) concerns the evaluation of both the ICDR (LSA-420) and the CDR (LSA-454). The characteristics of AVHRR-based vegetation indices provided by the LSA-SAF are described in the Product User Manual (PUM) and in more detail in the ATBD. An overview of the ENDVI10 Product Requirements is given in Table 1. Further details on the LSA-SAF product requirements can be found in the Product Requirements Document (PRD), available at the LSA SAF website at <http://landsaf.ipma.pt>.

Although validation of the ENDVI v2 CDR should normally comprise the entire archive (2008 – present), this was not possible, due to the fact that the migration of the processing chain to the VITO MEP environment, its implementation and testing, as well as the set-up of an acceptance environment, took more time than expected. Nevertheless, this Validation Report will provide ENDVI v2 inter-comparisons for all three MetOp platforms and spans the period 2016 – 2019.

The VR document’s objectives are as follows:

1. To provide a quality assessment of the ENDVI10 v2, by intercomparison to ENDVI10 v1 and the Copernicus Global Land Service (CGLS) NDVI v2.2. Intercomparison is performed at a global extent, as well as for separate biomes and specific sites.
2. To obtain an indication on the consistency of ENDVI10 v2 over the three MetOp platforms. For this reason, an intercomparison of MetOp-B ENDVI10 v2 with its MetOp-A and -C counterparts for 2016 and 2019, respectively, was carried out.

The validation focuses on product completeness, spatial, statistical, and temporal consistency. The validation methods are described in Chapter 2. The results of the quality assessment of ENDVI10 v2 are described in Chapter 3. Chapter 4 describes the radiometric consistency and geometric consistency between MetOp-A, -B and -C. Chapter 5 formulates a summary and conclusions.

Table 1. Product Requirements for ENDVI10, in terms of area coverage, resolution, and accuracy. R^2 denotes the coefficient of determination (explained variance) between paired (same day and cloud/snow-free) observations of MetOp-AVHRR and SPOT-VGT / PROBA-V. When this is not possible, R^2 is estimated from matches of 10-day composites with the respective ENDVI10 10-day synthesis.

Product Name	Product Identifier	Coverage	Resolution		Accuracy		
			Temporal	Spatial	Threshold	Target	Optimal
ENDVI10	LSA-454 LSA-420	Global	10-daily	1km	$R^2 > 0.80$	$R^2 > 0.90$	$R^2 > 0.95$

1.6 Related documents

The following documents are baseline references which provide complementary information, evaluation evidences and conclusions on the performance of the algorithms:

- i. ATBD ENDVI10 version 2
- ii. PUM ENDVI10 version 2
- iii. VR ENDVI10 version 1
- iv. ATBD ENDVI10 version 1

2 Validation methods

2.1 Overall procedure

The quality assessment of the ENDVI10 v2 is based on the comparison of the ENDVI10 v2 product with ENDVI10 v1 and CGLS NDVI v2.2 over a 3 year period (2016-2018). The products are analyzed at global scale and for time series analyses over the Benchmark Land Multisite Analysis and Intercomparison of Products (BELMANIP)2/Direct sites. Although the NDVI is not a biophysical variable, the validation is performed following the guidelines, protocols, and metrics defined by the Land Product Validation (LPV) group of the Committee on Earth Observation Satellite (CEOS) for the validation of satellite-derived land products (LPV) for the indirect validation of similar products. CEOS/LPV is currently establishing specific protocols for vegetation index validation and intercomparison. Table 2 summarizes the overall procedure applied for the analysis. Only valid observations over land, with AOT below AOT_{max} are considered (i.e. with resp. status map bits 6, 7 and 4 raised). Observations with status map bits 0 (snow), 1 (cloud) and/or 2 (cloud or shadow) raised are excluded from the analysis.

Table 2. Overall procedure for the quality assessment of ENDVI10 v2.

Criterion	Method and/or Validation metric
Product completeness	<ul style="list-style-type: none"> Temporal evolution of good values or pixels flagged as ‘valid’ over land at global scale Spatial distribution of missing values or pixels flagged as ‘invalid’ over land at global scale Frequency distribution of the length of the gaps (in dekads) at global scale
Spatial consistency	<ul style="list-style-type: none"> Frequency histograms of ENDVI10 v2, ENDVI10 v1 and CGLS NDVI v2.2 per biome Spatial distribution of the validation metrics expressing the similarities/differences between ENDVI10 v2 and ENDVI10 v1 at global scale Spatial distribution of the validation metrics expressing the similarities/differences between ENDVI10 v2 and CGLS NDVI v2.2 at global scale. Comparison with ENDVI10 v1 vs. CGLS NDVI v2.2
Statistical consistency	<ul style="list-style-type: none"> Scatterplots (incl. GMR equation, R^2) between ENDVI10 v2 and ENDVI10 v1, overall and per biome, at global scale Scatterplots (incl. GMR equation, R^2) between ENDVI10 v2 and CGLS NDVI v2.2, overall and per biome, at global scale. Comparison with ENDVI10 v1 vs. CGLS NDVI v2.2
Temporal consistency	<ul style="list-style-type: none"> Frequency distribution of the temporal smoothness at global scale: the temporal smoothness is evaluated by taking three consecutive observations and computing the absolute value of the different delta between the center $P(d_{n+1})$ and the corresponding linear interpolation between the two extremes $P(d_n)$ and $P(d_{n+2})$ as follows: $\delta(d_n) = \left P(d_{n+1}) - P(d_n) - \frac{P(d_n) - P(d_{n+2})}{d_n - d_{n+2}}(d_n - d_{n+1}) \right$ Temporal variations and realism: temporal profiles of ENDVI10 v2, ENDVI10 v1 and CGLS NDVI v2.2 are extracted over BELMANIP2/Direct sites.

Furthermore, to evaluate the radiometric consistency between MetOp-A, -B and -C, intercomparison is done on ENDVI10 v2 derived from MetOp-A and -B over January-December

2016, and on ENDVI10 v2 derived from MetOp-B and -C over the period July-September 2019. This analysis is restricted to statistical consistency analysis, consisting of scatterplots between ENDVI10 v2 based on different input sensors at global scale, and bias frequency histograms. In addition, Hovmöller plots are created to intercompare a continuous series MetOp-A/B/C with CGLS NDVI v2.2. Finally, in order to evaluate the geometric accuracy the geolocation the ENDVI10 v2 is compared to a number of globally distributed Ground Control Points (CGPs).

The following paragraphs describe the methods used. The validation metrics and Geometric Mean Regression (GMR) used are described in section Section 2.2. The sampling design is explained in Section 2.3. The method used to evaluate geometric accuracy is described in Section 2.4. Satellite reference data products that are used to compare the ENDVI10 v2 to are described in Section 2.5. Finally, the way regional and biome assessment is performed is summarized in Section 2.6.

2.2 Validation metrics

In the following paragraphs and equations, X refers to the dataset to be validated in this case ENDVI10 v2, and Y to the reference dataset.

2.2.1 Coefficient of determination (R^2)

The coefficient of determination (R^2) indicates the agreement or covariation between two datasets with respect to a linear regression model. It summarizes the total data variation explained by this linear regression model. The result varies between 0 and 1, with higher R^2 values indicating higher covariation between the datasets. In order to detect a systematic difference between the two datasets, the regression line coefficients should be used. A disadvantage of using R^2 is that it only measures the strength of the relationship between the data, but gives no indication when the data series have similar magnitude (Duveiller et al., 2016a).

$$R^2 = \left(\frac{\sigma(X,Y)}{\sigma(X) \cdot \sigma(Y)} \right)^2 \quad (\text{Eq. 2})$$

with $\sigma(X)$ and $\sigma(Y)$ the X and Y standard deviation and $\sigma(X,Y)$ X and Y covariation, respectively. The R^2 is only provided together with the regression analysis in the global statistical analysis (see below), because it allows for a quantitative interpretation of the scatterplots.

2.2.2 Geometric mean regression

The geometric mean (GM) regression model is used to identify the relationship between two datasets. Because both datasets are subject to noise, it is most appropriate to use an orthogonal (model II) regression like the GM regression. By applying an eigen decomposition to the X and Y covariance metrics, two eigenvectors are obtained, which describe the principal axes of the point cloud (Duveiller et al., 2016b), i.e., the regression line with equation:

$$Y = a + b \cdot X \quad (\text{Eq. 3})$$

The GM regression slope and intercept are added as quantitative information related to the scatterplots. The regression is also used to derive the agreement coefficient and to differentiate between systematic and random differences, as described in the next paragraphs.

2.2.3 The root mean squared difference (RMSD)

The Root Mean Squared Difference (RMSD) measures how much the difference between the two datasets deviates from 0 and is defined as:

$$RMSD = \sqrt{\frac{1}{n} \sum_{i=1}^n (X_i - Y_i)^2} \quad (\text{Eq. 4})$$

The *RMSD* is an expression of the overall difference, including random and systematic differences (see below).

2.2.4 Random and systematic differences (RMPDu and RMPDs)

The random and systematic differences are derived from the mean squared difference (*MSD*), defined as:

$$MSD = \frac{1}{n} \sum_{i=1}^n (X_i - Y_i)^2 \quad (\text{Eq. 5})$$

The *MSD* is further partitioned into the systematic mean product difference (*MPD_s*) and the unsystematic or random mean product difference (*MPD_u*). To be comparable to the *RMSD* in terms of magnitude, the square root of the systematic and unsystematic mean product differences are used (*RMPD_s* and *RMPD_u*):

$$RMPD_u = \sqrt{\frac{1}{n} \sum_{i=1}^n (|X_i - \hat{X}_i|)(|Y_i - \hat{Y}_i|)} \quad (\text{Eq. 6})$$

with \hat{X}_i and \hat{Y}_i estimated using the GM regression line and n the number of samples.

$$RMPD_s = \sqrt{MSD - MPD_u} \quad (\text{Eq. 7})$$

The partitioning of the difference into systematic and unsystematic difference provides additional information to the *RMSD* on the nature of the difference between two datasets.

2.2.5 Mean Bias Error (MBE)

The Mean Bias Error (MBE) is defined as the actual difference between two data sets and positive and negative differences between observations:

$$MBE = \frac{1}{n} \sum_{i=1}^n (X_i - Y_i) = \bar{X} - \bar{Y} \quad (\text{Eq. 8})$$

2.3 Sampling

The global images are systematically sub-sampled, taking the central pixel in a window of 21×21 pixels. This subsample is representative for the global vegetation patterns and considerably reduces processing time, while retaining the relation between the observation and its viewing and illumination geometry.

By default, only clear observations are used in the analyses. This means that only observations that are not identified as bad observation (cloud/shadow/snow/unreliable) in the Status Map are analyzed (see above). However, for the pairwise comparison between ENDVI10 v2 and ENDVI10 v1, and between ENDVI10 v2 based on different input sensors (MetOp-A/B and MetOp-B/C), an additional sampling is done, with the purpose of controlling the selection of clear observations being of the same date and/or an as similar as possible observation geometry to reduce anisotropy effects. The following constraints are used:

- **‘ViewAngle’**: In the pairwise comparison, only observations with Viewing Zenith Angles (VZA) < 30° and with same viewing direction, i.e., either in backscatter or forward scatter, are used.
- **‘IllumAngle’**: In the pairwise comparison only observations with solar zenith angles (SZA) < 30° are used. The SMAC algorithm is more reliable for lower SZA.
- **‘ViewAngle+IllumAngle’**: In the pairwise comparison a combination of both the ‘ViewAngle’ and ‘IllumAngle’ constraints are applied.

In order to verify the temporal or spatial bias in the sample retained after applying the additional data sampling, this was further investigated.

Figure 1 shows the temporal evolution of the number of observations retained after applying the sampling schemes on the Intercomparison between ENDVI10 v2 and ENDVI10 v1. Figure 2 indicates the global distribution of retained observations. Using the ‘ViewAngle’ scheme, even in the winter period about 30% of the observations are retained globally. The largest amount of observations are selected over deserts (due to little cloud cover) and the smallest amount over high latitudes and areas with large cloud and/or snow cover. However, when constraints are applied on the SZA, as in the ‘IllumAngle’ and ‘ViewAngle+IllumAngle’ scheme, very few observations are retained, only during the Northern hemisphere summer months. In addition, the spatial distribution of retained observations per sampling scheme indicates that only pixels between roughly 12° – 43°N are included. Therefore the results based on these sampling schemes must be treated with caution, as they are not representative for the global, full year sample.

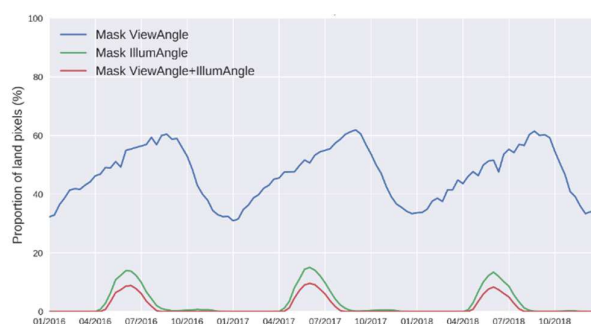


Figure 1. Temporal evolution over 2016 – 2018 of the global number of observations [%] retained after additional sampling for the ‘ViewAngle’, ‘IllumAngle’ and ‘ViewAngle+IllumAngle’ sampling schemes for the Intercomparison between ENDVI10 v2 and ENDVI10 v1.

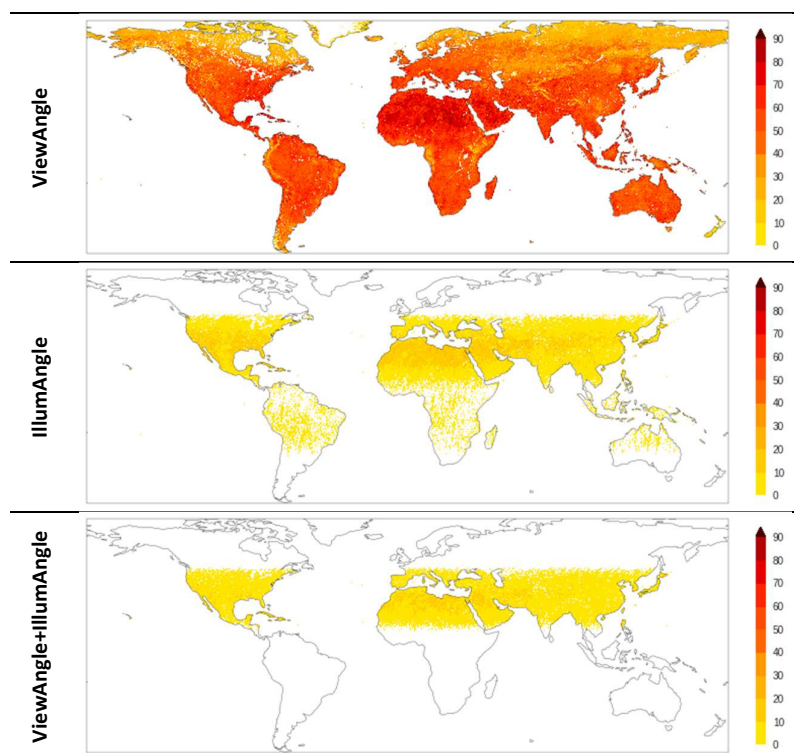


Figure 2. Spatial distribution of the number of observations (%) retained after additional sampling for the 'ViewAngle', 'IllumAngle' and 'ViewAngle+IllumAngle' sampling schemes over 2016 – 2018 for the Intercomparison between ENDVI10 v2 and ENDVI10 v1.

A similar analysis was done for the intercomparison between ENDVI10 v2 based on MetOp-A vs. MetOp-B (January-December 2016) and the intercomparison between MetOp-B and MetOp-C (July-September 2019), in order to minimize the effects of different viewing angles on the analysis of radiometric consistency, see respectively Figure 3-Figure 4 and Figure 5-Figure 6. It is to be noted that – related to the shifted orbits between MetOp-A, -B and -C – few observations remain after applying the 'ViewAngle' constraint. The 'IllumAngle' and combined sampling are therefore not applied. Because the sample after applying the 'ViewAngle' constraint is small, the results should be treated with caution.



Figure 3. Temporal evolution over January-December 2016 of the global number of observations [%] retained after additional sampling for the 'ViewAngle' sampling scheme for the Intercomparison between ENDVI10 v2 based on MetOp-A and MetOp-B.

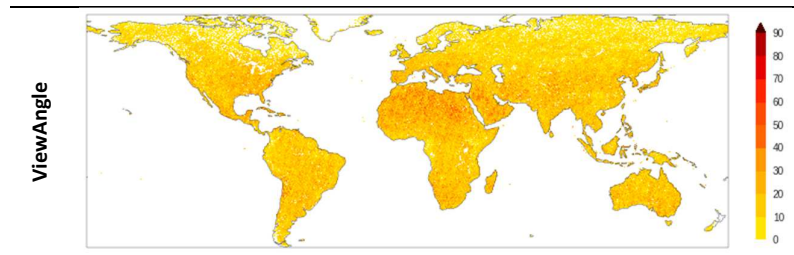


Figure 4. Spatial distribution of the number of observations (%) retained after additional sampling for the 'ViewAngle' sampling schemes over January-December 2016 for the Intercomparison between ENDVI10 v2 based on MetOp-A and MetOp-B.

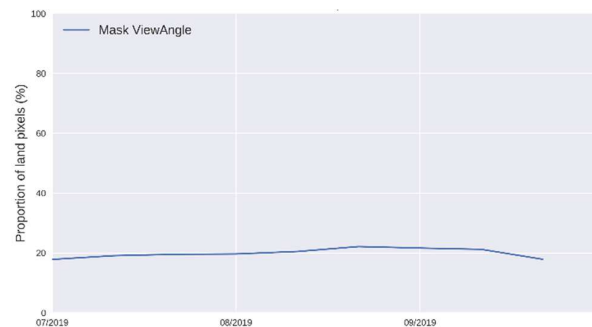


Figure 5. Temporal evolution over July-September 2019 of the global number of observations [%] retained after additional sampling for the 'ViewAngle' sampling scheme for the intercomparison between ENDVI10 v2 based on MetOp-B and MetOp-C.

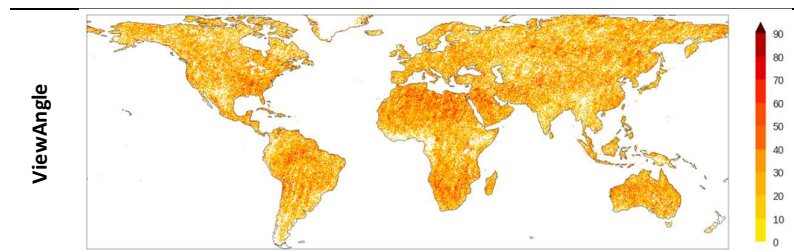


Figure 6. Spatial distribution of the number of observations (%) retained after additional sampling for the 'ViewAngle' sampling scheme over July-September 2019 for the Intercomparison between ENDVI10 v2 based on MetOp-B and MetOp-C.

2.4 Geometric accuracy

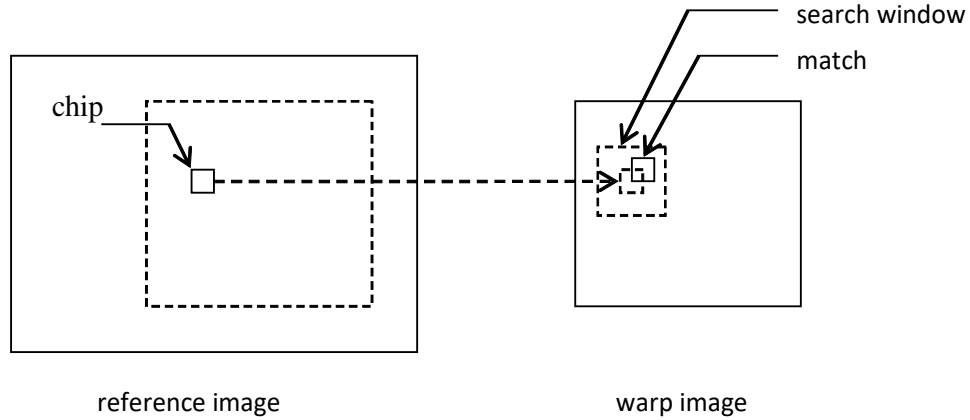
The geometric accuracy of the ENDVI10 v2 data product is validated using a chipmatching method, using monthly SPOT-VGT composites (1999 – 2006) as reference. A chip is defined as a small image subset with a certain amount of points, the Ground Control Points (GCPs), with known and stable geolocation. The geolocation validation is then performed as follows:

- Select a chip position (using a list of predefined chip positions or using a random number generator).

- Map the chip position to the reference window and retrieve the $N_1 \times N_1$ chip window from the reference image.
- Map the chip position to the warped image, giving (x_0, y_0) , and search the position (x_1, y_1) in a $N_2 \times N_2$ search window for which the correlation between the warp image and the chip image is maximal.
- A match is found if certain conditions are fulfilled, e.g. the correlation value has to be above a certain threshold, the correlation peak has to be sharp enough, etc.
- Repeat the above steps until N matching chips have been found and determine the polynomials $f_x(x, y)$ and $f_y(x, y)$ that map the (x_1, y_1) coordinates into (x_0, y_0) coordinates:

$$f_x(x_1, y_1) = x_0$$

$$f_y(x_1, y_1) = y_0$$
- Generate the warped image using the polynomials f_x and f_y to determine for each pixel position of the warped image the corresponding 'nearest neighbour' pixel in the warp image. Only the tiles with a sufficient fill level are warped and the others are removed from the image.



The accuracy of the warp image is calculated from the (x_0, y_0) and (x_1, y_1) coordinates of the N matching chips:

$$Acc = \frac{\sum [(x_1, y_1) - (x_0, y_0)]}{N} \quad (\text{Eq. 9})$$

The Root Mean Square Error (RMSE) provides a measure for the accuracy of the warping and is calculated as:

$$RMSE = \sqrt{\frac{\sum [(f_x(x_1, y_1) - x_0)^2 + (f_y(x_1, y_1) - y_0)^2]}{N}} \quad (\text{Eq. 10})$$

2.5 Satellite reference products

2.5.1 LSA SAF – ENDVI10 version 1 based on MetOp/AVHRR (ENDVI10 v1)

The LSA-SAF ENDVI10 version 1 is described in the ATBD ENDVI10 version 1. The only difference compared to ENDVI10 version 2 is the AOT input that is used in the atmospheric correction (see also Section 1).

2.5.2 Copernicus GLS – NDVI v2.2 based on PROBA-V (CGLS NDVI v2.2)

From 1 January 2013, the Copernicus Global Land Service (CGLS)¹ is continuously providing a set of biophysical variables describing the vegetation dynamics, the energy budget at the continental surface, and the global water cycle. The service performs the timely production, re-processing, archival, and distribution of quality-checked products.

The CGLS NDVI 1km v2.2 is an operational global product with temporal coverage from April 1998 – present. The time series includes data from different sensors, i.e., SPOT4-VGT1 (May 1998 – January 2003), SPOT5-VGT2 (February 2003 – December 2013) and PROBA-V (January 2014 – present). The reprocessed SPOT-VGT data (Collection 3) and PROBA-V (Collection 1) are used in NDVI v2.2 and a spectral harmonization is applied on the NDVI derived from SPOT4-VGT1.

The data used in this study (2016-2019) are solely based on PROBA-V. The CGLS NDVI 1km v2.2 is hereafter named ‘CGLS NDVI v2.2’.

2.6 Regional/Biome assessment

2.6.1 Stratification per biome

An aggregated version of the Global Land Cover 2000 (GLC2000) classification (Bartholomé and Belward, 2005) was used to distinguish between major land cover classes at global scale (Figure 7). The classes were aggregated according to the scheme in Table 3.

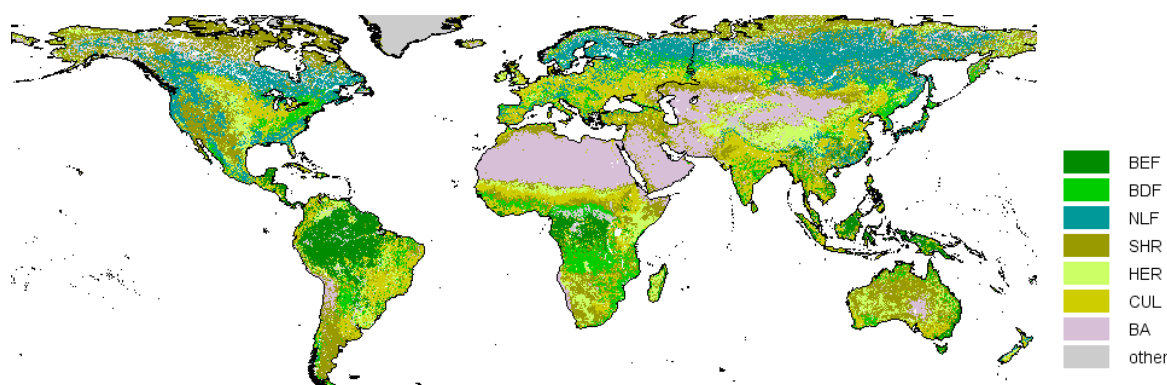


Figure 7. The GLC classification aggregated into 7 classes.

¹ <https://land.copernicus.eu/global/index.html>

Table 3. Aggregation scheme for GLC2000 classes into 7 major biomes and proportion of each biome at global scale.

Abbreviation	Name	GLC2000 classes	Proportion at global scale
BEF	Broadleaved Evergreen Forests	1	7%
BDF	Broadleaved Deciduous Forests	2-3	7%
NLF	Needle-leaved Forests	4-5	16%
SHR	Shrubland	11-12, 14	23%
HER	Herbaceous cover	13	10%
CUL	Cultivated areas and cropland	16-18	16%
BA	Bare areas	19	13%
Other (not considered in the analyses)		6-10, 15, 20-22	8%

2.6.2 BELMANIP2 and DIRECT sites

BELMANIP2 and DIRECT sites are used to evaluate the temporal realism of the ENDVI10 v2 time series in comparison with those for ENDVI10 v1 and CGLS NDVI v2.2. BELMANIP2.1 is a collection of sites originating from existing experimental networks (FLUXNET, AERONET, VALERI, BigFoot, etc.) that are completed with sites selected from the GLOBCOVER vegetation land cover map in order to obtain a global representation (see Figure 8). It is an improved version of the original BELMANIP sites (Baret et al., 2006). DIRECT is a collection of sites for which ground measurements are available and that have been collected (Garrigues et al., 2008) and processed according to the CEOS-LPV guidelines (NASA, 2014).

In order to evaluate temporal realism and qualitatively compare between products, temporal profiles are extracted for all BELMANIP2 and DIRECT sites (Figure 8). Ad hoc examples will be selected based on expert knowledge to illustrate the temporal realism of the product time series.

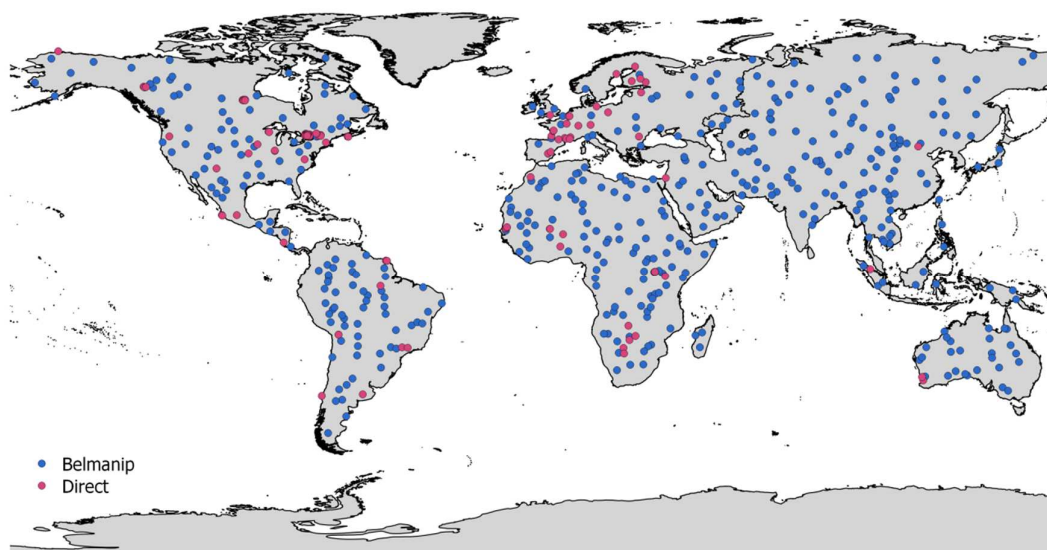


Figure 8. Spatial distribution of the BELMANIP2 (blue) and DIRECT (pink) sites.

2.6.3 Latitude bands

A map of latitude bands of 6° wide (Figure 9) is used in order to enable spatio-temporal analysis and the creation of Hovmöller plots based on spatially subsampled global images. Figure 9 shows the latitude bands and the number of land pixels included in each band.

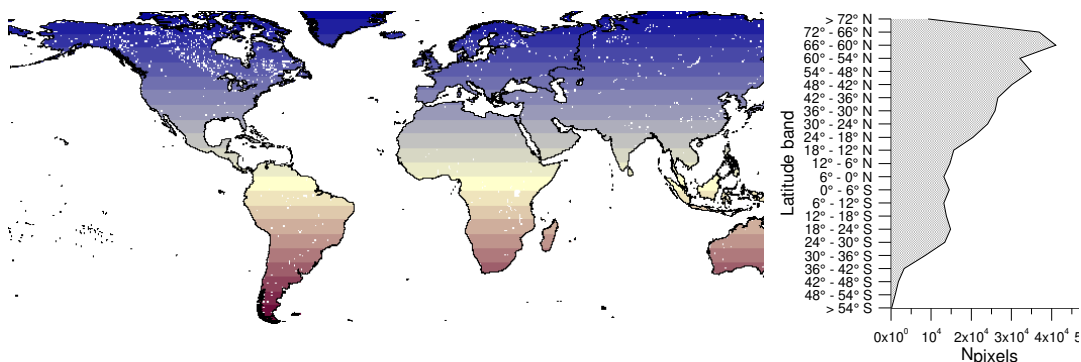


Figure 9. Latitude bands used for spatio-temporal analysis (left) and number of pixels per band (right)

3 Validation of ENDVI10 v2

The validation results below describe the results of the quality assessment of ENDVI10 v2 based on MetOp-B input (at the time of writing the nominal MetOp satellite) for the period 2016-2018. The various validation criteria, presented in Table 2, were obtained through inter-comparisons with ENDVI10 v1 and PROBA-V CGLS NDVI v2.2.

3.1 Product completeness

3.1.1 Temporal evolution of product completeness

Figure 10 shows the temporal behavior of the product completeness for ENDVI10 v2, ENDVI10 v1, and CGLS v2.2. ENDVI10 observations are considered as 'valid' when status map bits 6 (valid observation), 7 (land) and 4 (AOT below AOT_{max}) are raised and status map bits 0 (snow), 1 (cloud) and/or 2 (cloud or shadow) are not raised.

All three datasets show the same temporal signature, that is, a minimum completeness during the northern hemisphere winter months (December - February) and a maximum during the northern hemisphere summer.

Over 2016 – 2018, the average good observation amount is 70.7% for ENDVI10 v2, 71.0% for ENDVI10 v1, and 74.0% for CGLS NDVI v2.2. The higher value for CGLS can be attributed to the later overpass time for PROBA-V and the wider swath compared to MetOp-B-AVHRR (see Annex 1). Although the yearly average for ENDVI10 v2 and v1 is almost the same, for some dekads a difference in product completeness of a few percent can be seen. An analysis on dekads for which the difference in product completeness between ENDVI10 v2 and v1 was $> 0.5\%$ revealed that the missing observations in ENDVI10 v2 contain 'cloud' or 'snow' observations in the majority of cases. Based on the analysis of spatial distribution (see §3.1.2), it is clear that this difference is mainly observed over New Zealand. Unfortunately, the root cause of this issue had not been found yet at the time of writing and requires additional investigation.

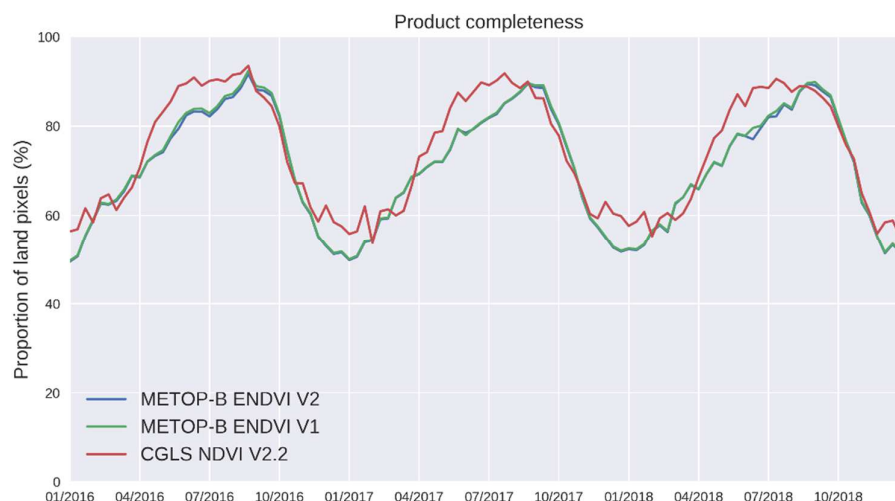


Figure 10. Temporal evolution of the amount of good observations over 2016 – 2018 at global scale for ENDVI10 v2 (blue), ENDVI10 v1 (green) and CGLS NDVI v2.2 (red).

3.1.2 Spatial distribution of product completeness

Figure 11 shows the spatial distribution of the product completeness for ENDVI10 v2, ENDVI10 v1, and CGLS NDVI v2.2 over 2016 – 2018. For all datasets, the amount of missing values increases when going northward, with >50% missing for latitudes >60°. In ENDVI10 v2 and v1, some distinct areas with relatively large amounts of missing values are seen over eastern and equatorial Africa, the northern Andes, south-east Asia, and Siberia. These areas are to a certain extent visible in the CGLS v2.2 dataset, although the magnitude differs, probably due to the shorter revisit time for PROBA-V related to the larger swath of the sensor (see Annex 1) and to the lack of thermal bands that limits an accurate cloud detection. The CGLS v2.2 dataset has considerably lower completeness at higher latitudes. This is caused by an artifact in the cloud detection of PROBA-V over these regions².

Overall, the spatial patterns for ENDVI10 v2 and v1 are very similar, except for New Zealand, where ENDVI10 v2 shows a much lower product completeness. As described in the previous paragraph, this issue needs further investigation. Figure 12 shows a difference map of product completeness (ENDVI10 v2 minus ENDVI10 v1) over 2016 – 2018. Apart from the larger difference over New Zealand, small differences – mainly located in Asia – occur, related to the higher AOT input used in this region in the atmospheric correction of ENDVI10 v2 (see also Annex 2).

² See <http://proba-v.vgt.vito.be/en/quality/known-issues>

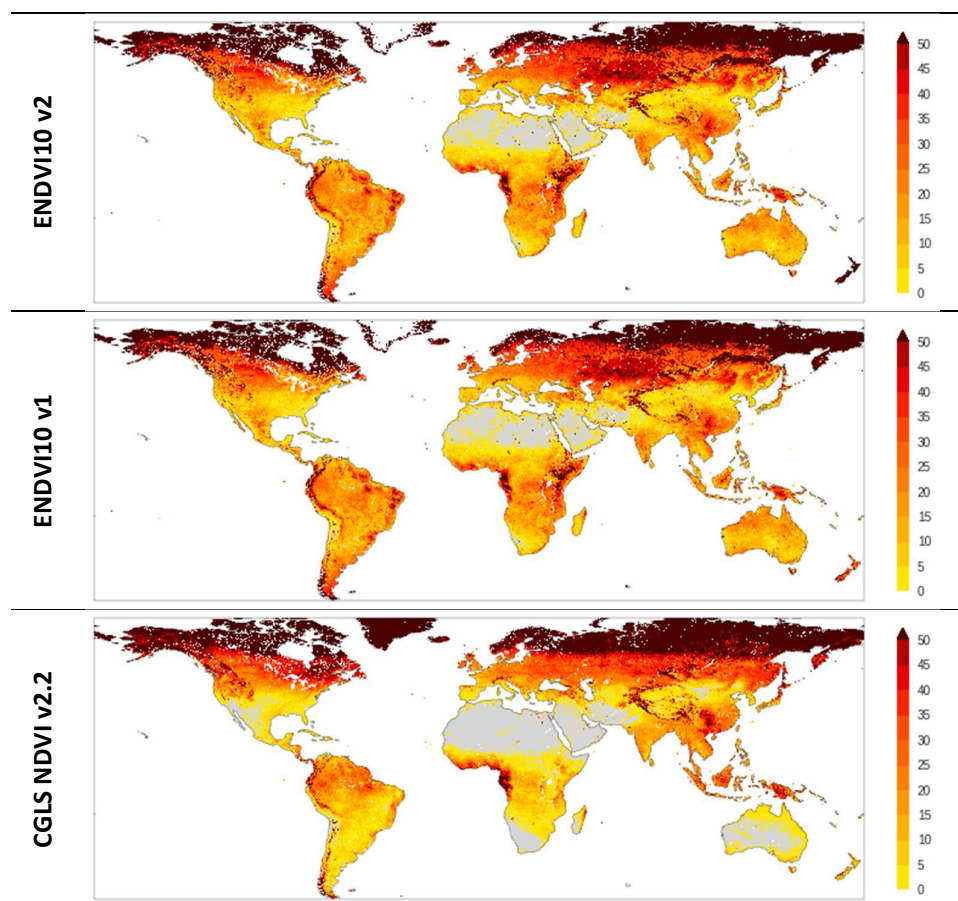


Figure 11. Spatial distribution of missing values occurrence frequency (%) over 2016 – 2018 for ENDVI10 v2 (top), ENDVI10 v1 (middle) and CGLS NDVI v2.2 (bottom).

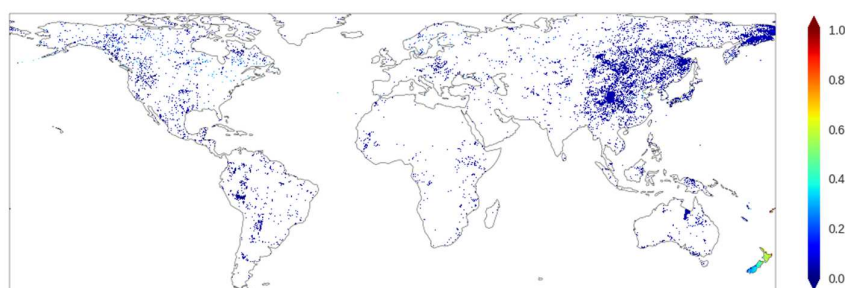


Figure 12. Difference in spatial distribution of missing values occurrence frequency between ENDVI10 v2 and ENDVI10 v1 (%) over 2016 – 2018.

3.1.3 Gap length frequency

Figure 13 shows for ENDVI10 v2, ENDVI10 v1, and CGLS NDVI v2.2 the frequency distribution of the gap length, a metric that expresses the amount of missing consecutive dekads. The distribution is very similar for ENDVI10 v2 and ENDVI10 v1. CGLS NDVI v2.2 shows less short gaps, but the occurrence of longer gap lengths is slightly larger, most probably related to the cloud

detection issue in PROBA-V (see also §3.1.2). All datasets show a sharp decrease between 1 and 3 dekads.

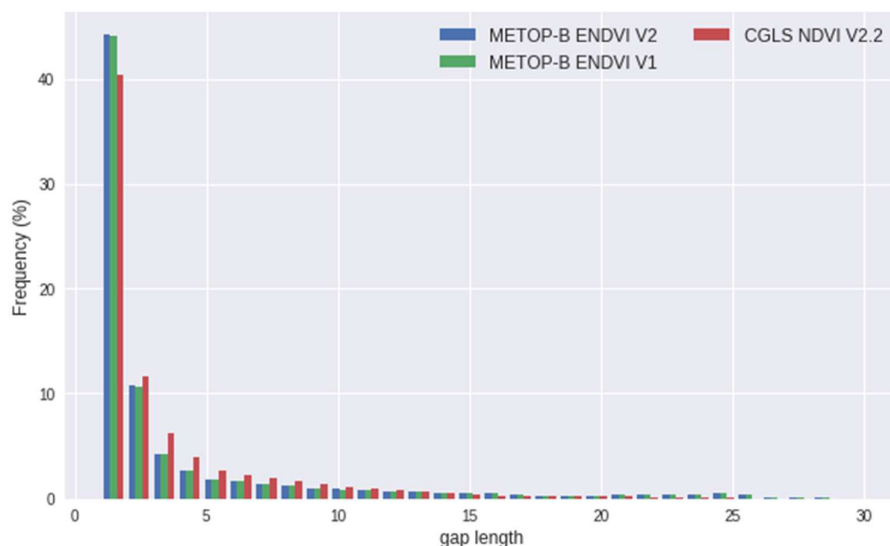


Figure 13. Frequency distribution of the gap length (in dekads) over 2016 – 2018 at global scale for ENDVI10 v2 (blue), ENDVI10 v1 (green) and CGLS NDVI v2.2 (red).

3.2 Spatial consistency

3.2.1 Histograms per biome

Figure 14 presents the NDVI frequency distributions for ENDVI10 v2, ENDVI10 v1 and CGLS NDVI v2.2 for the 7 defined biomes (see Section 2.6.1). In general, the distributions are similar in shape.

Compared to ENDVI10 v1, ENDVI10 v2 shows slightly lower frequencies of the highest NDVI ranges for BEF and BDF. The opposite is true for NLF. There is a slight shift towards lower NDVI values for SHR, HER, BA and CUL.

CGLS NDVI v2.2 in general shows a larger range of NDVI values, with higher frequencies of high NDVI values (for BEF, BDF, NLF and CUL), and higher frequencies for lower NDVI values (as for NLF, SHR, HER, CUL and BA). The observed differences are resulting from a complex combination of (1) differences in sensor characteristics, such as Spectral response function (SRFs) defining the spectral range that is measured and the Point Spread Function (PSF) that defines the area that is sensed per pixel, (2) the difference in absolute radiometric calibration, (3) different processing choices, e.g. different atmospheric correction inputs, and (4) directional effects due to the difference in swath width and overpass time.

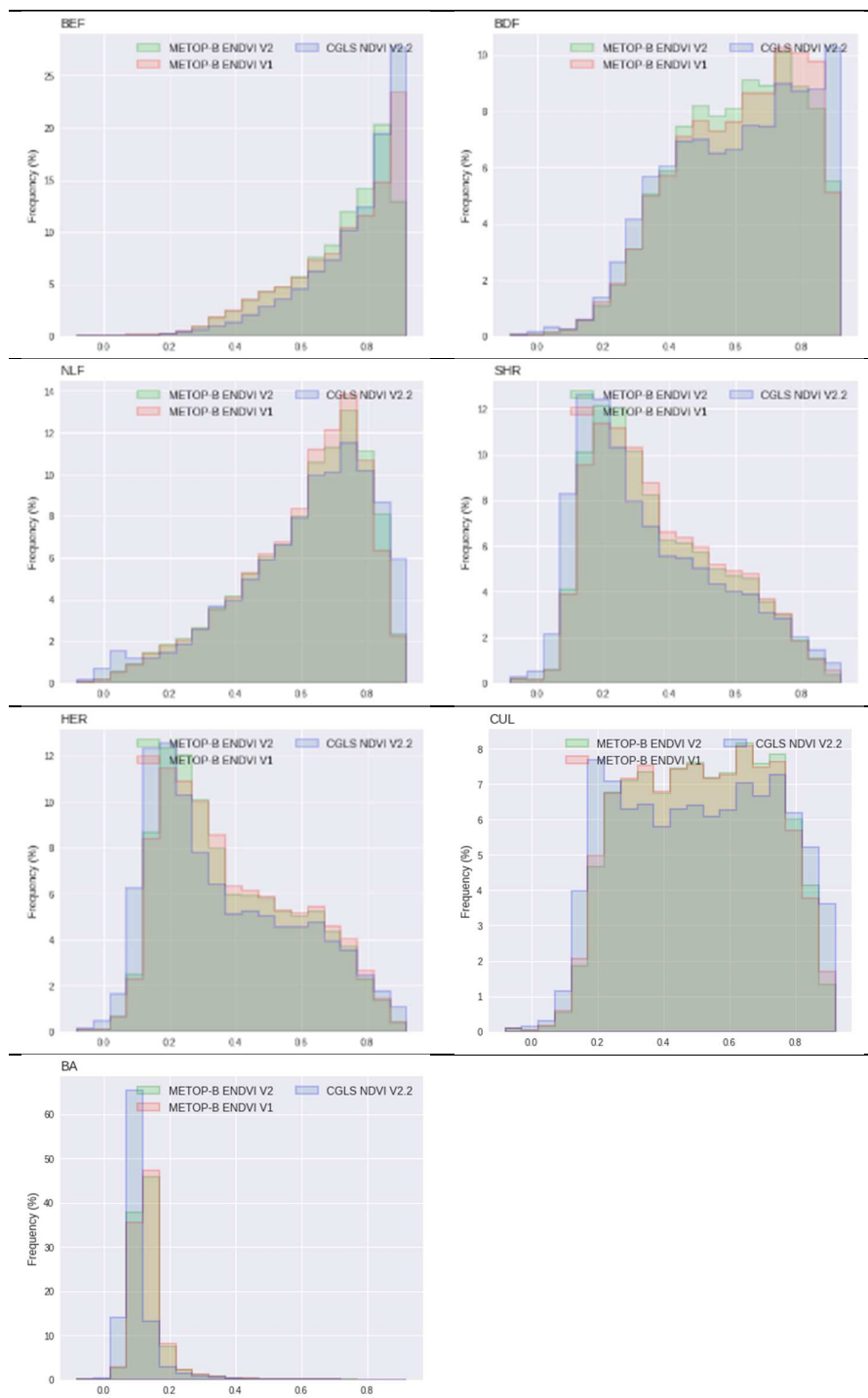


Figure 14. Frequency distributions over 7 different biomes. Pairwise comparison of physical NDVI values for ENDVI10 v2 (green), ENDVI10 v1 (red) and CGLS NDVI v2.2 (blue) over 2016-2018. X-axis: NDVI values with bin sizes of 0.1, Y-axis: occurrence frequency [%].

3.2.2 Spatial distribution of validation metrics

Figure 15 shows the spatial distribution of the *RMSD*, as well as its systematic (*RMPDs*) and unsystematic (*RMPDu*) components for the pixelwise pairwise comparison between ENDVI10 v2 and ENDVI10 v1. Over large parts of the globe, the *RMSD* is roughly below 0.04. However, over Central Africa, northern India and the Himalaya, as well as east Asia *RMSD* values of up to > 0.10 are visible. For the latter area, the high *RMSD* is more systematic (see the large *RMPDs* values in the middle panel), while for the other areas mentioned above the random component is contributing most to the total *RMSD*.

The differences over these areas are related to the differences between the AOT datasets used in v2 and v1. The largest differences occur over those areas where the difference between the CAMS_{CLIM} AOT and the static latitudinal function are largest. Annex 2 shows for 4 dekads the difference between the CAMS_{CLIM} AOT and the static latitudinal AOT. The spatial agreement of the ENDVI10 v2 – v1 differences with the AOT differences can be seen by comparing Figure 15 with the plots in Annex 2. The very small dynamic range of the static latitudinal AOT (0.05 – 0.20) and the lack of regional differences translates into large differences over regions where the CAMS_{CLIM} data capture the regional AOT dynamics.

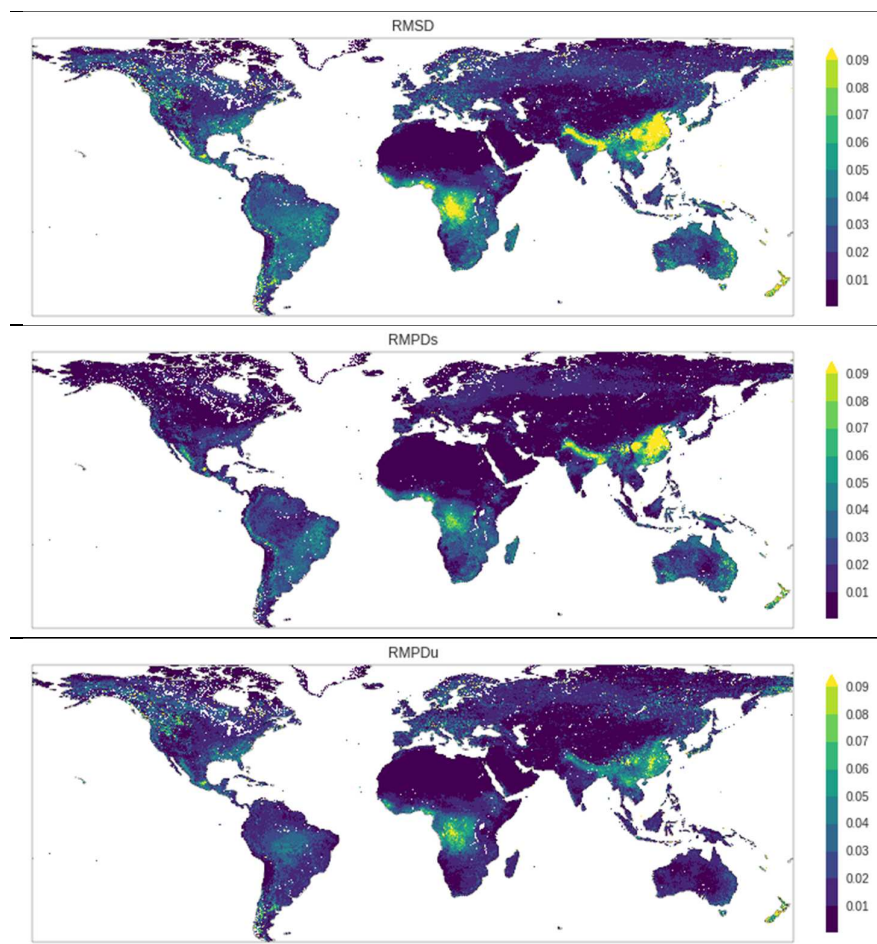


Figure 15. *RMSD*, *RMPDs* and *RMPDu* between ENDVI10 v2 and ENDVI10 v1 for MetOp-B, 2016 – 2018.

Figure 16 shows the *RMSD*, *RMPDs*, and *RMPDu* spatial distribution for ENDVI10 v2 vs CGLS NDVI v2.2 (left) and ENDVI10 v1 vs CGLS NDVI v2.2 (right). The largest *RMSD* values occur over north-western America, the Amazon basin, equatorial Africa, and South-East Asia. These differences result from among others the complex interaction between differences in absolute calibration, differences in atmospheric correction input datasets, directional effects, different performance of the cloud masking, and differences in SRFs.

The spatial distribution of the unsystematic difference suggests that undetected clouds in the CGLS NDVI v2.2 are the major contributing factor. Directional effects (mainly from the difference in viewing geometry) also contribute to the unsystematic difference. Note that the differences between CGLS NDVI v2.2 and ENDVI10 v1 resp. ENDVI10 v2 do not show the expected effect due to the difference in AOT input data between ENDVI10 v1 and v2. This is probably because other factors, such as those listed above, are more dominant.

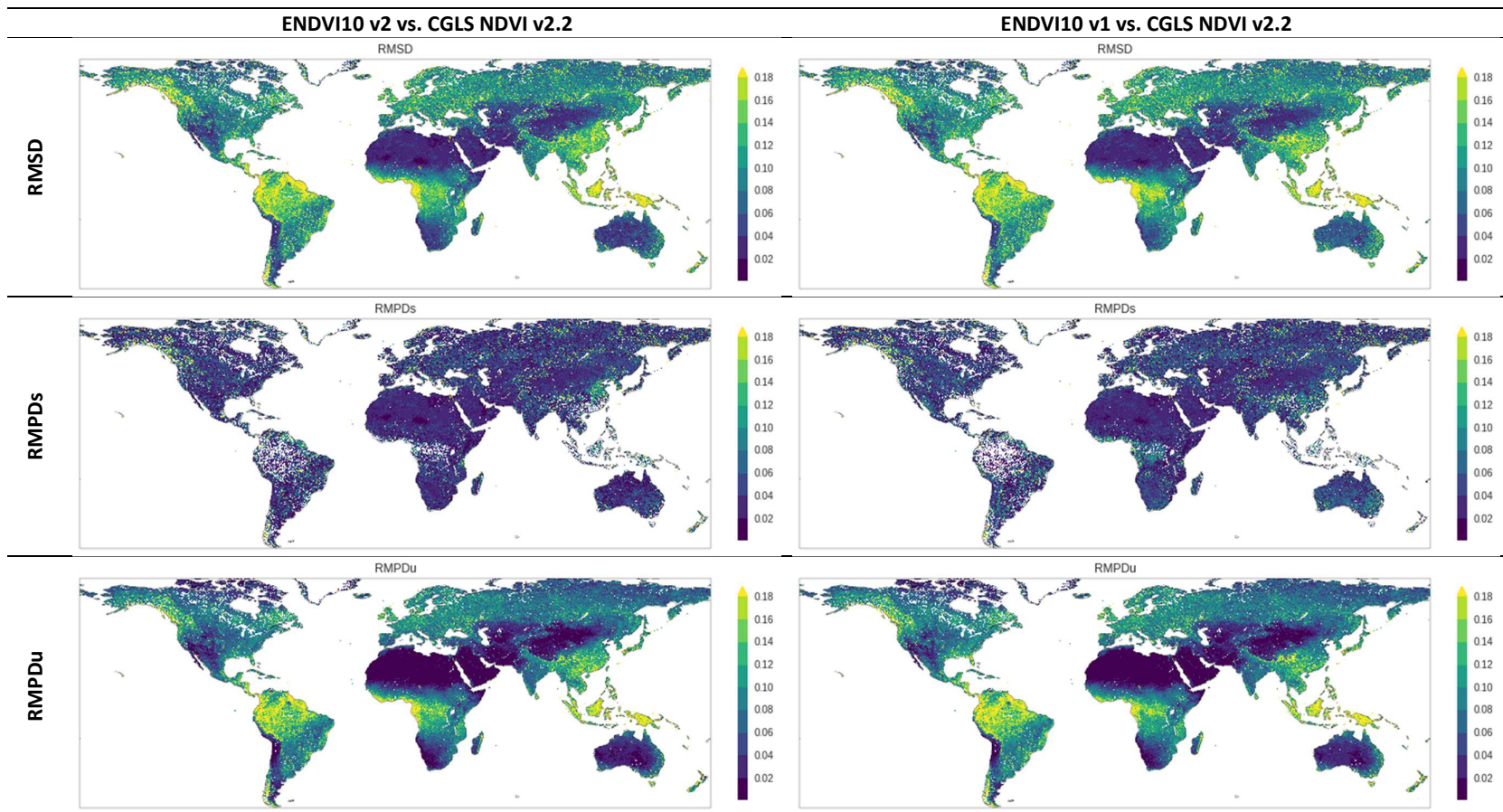
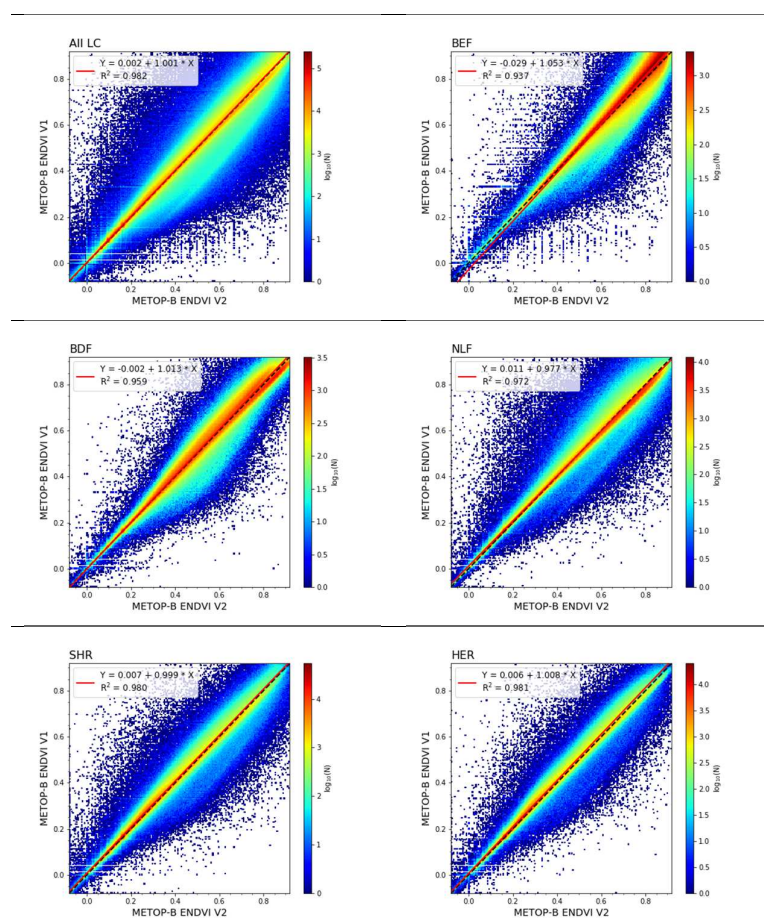


Figure 16. RMSD, RMPDs, and RMPDu between MetOp-B ENDVI10 v2 (left) and ENDVI10 v1 (right) and CGLS NDVI v2.2 for 2016 – 2018.

3.3 Statistical consistency

3.3.1 ENDVI10 v2 vs. ENDVI10 v1

Scatterplots of ENDVI10 v2 versus ENDVI10 v1 are presented in Figure 17. The upper left panel shows the aggregated results. The consistency between ENDVI10 v2 and v1 is very high, with $R^2=0.98$, a regression slope of 1.001, and a very small offset of 0.002. Nevertheless, it can be seen that slightly more scatter occurs below the 1:1 line, i.e., observations with higher NDVI values in ENDVI10 v2 compared to v1. The remaining panels show the comparisons ENDVI10 v2 vs v1 for the separate biomes. In general, differences are small, with slightly lower values of high ENDVI10 v2 values compared to v1 over the BEF and BDF biomes and the opposite over the NLF biome. Especially for CUL, but also visible in other plots, the majority of the samples coincide well with the 1:1 line, but the overall population is skewed to higher NDVI values for ENDVI10 v2. As explained before, the higher NDVI in ENDVI10 v2 is in line with the higher AOT values used for atmospheric correction, which results in a lower TOC RED reflectance and thus a higher NDVI.



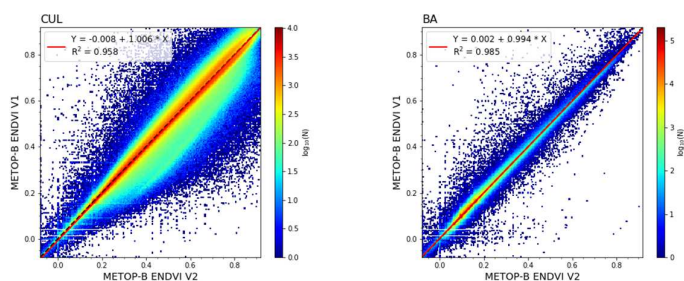
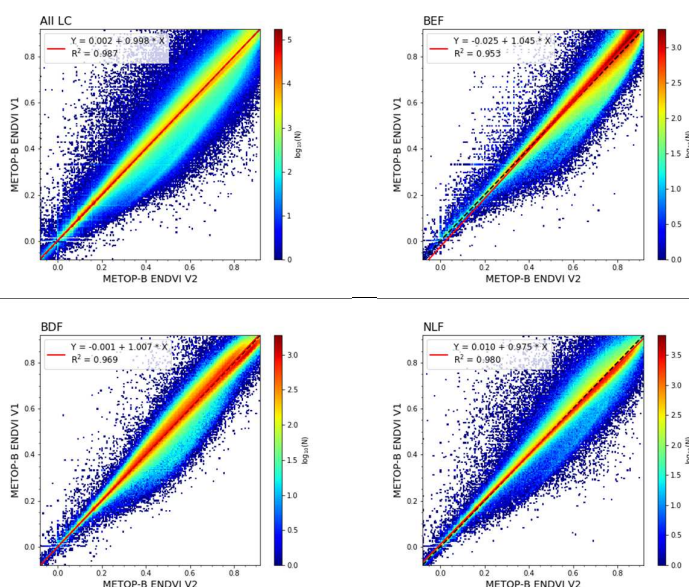


Figure 17. Scatterplots between ENDVI10 v2 (X) and ENDVI10 v1 (Y) over all land cover types (top left) and per biome at global scale. The dashed lines indicate the 1:1 relation, while the red solid lines denote the GM regression. Note the logarithmic color scale of the bin densities.

In order to obtain more insights on the cause of differences between ENDVI10 v2 and v1, the results were further analyzed using three additional sampling schemes ('ViewAngle', 'IllumAngle', and 'ViewAngle+IllumAngle') introduced in Section 2.3. The results are shown in Figure 18 – Figure 20. From these figures it follows that when applying additional sampling, the scatter decreases (compared to Figure 17), resulting in higher R^2 . In addition, the regression slope and intercept values slightly improve for all biomes, except for BA. However, the skewness towards higher ENDVI10 v2 NDVI values remains for all sampling schemes and for all vegetated biomes.



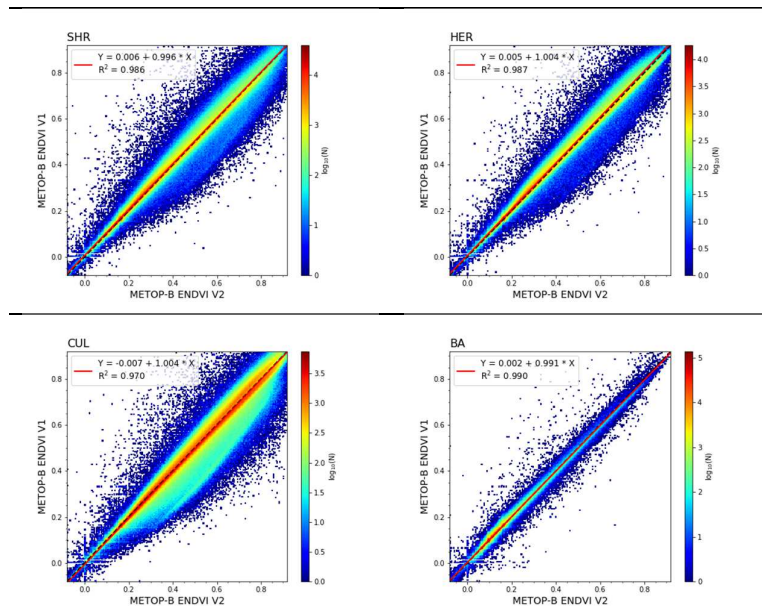
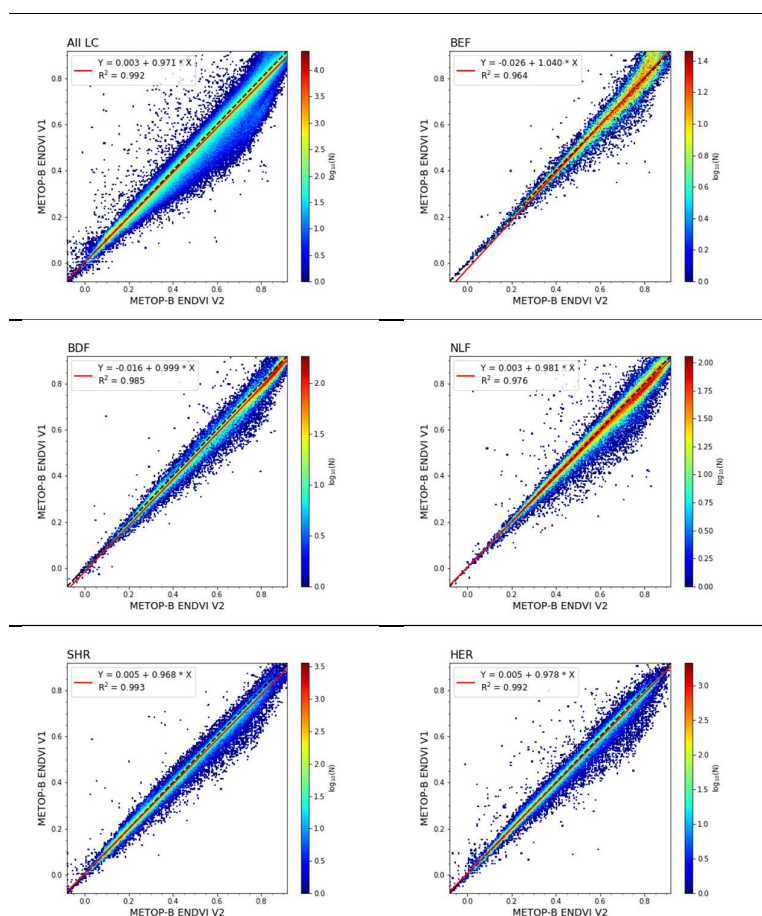


Figure 18. Scatterplots between ENDVI10 v2 (X) and ENDVI10 v1 (Y) over all land cover types (top left) and per biome at global scale, using the 'ViewAngle' sampling scheme.



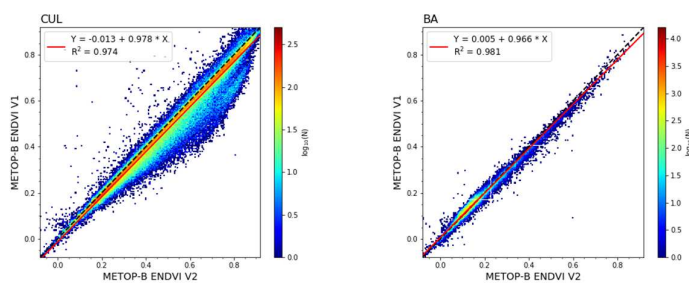
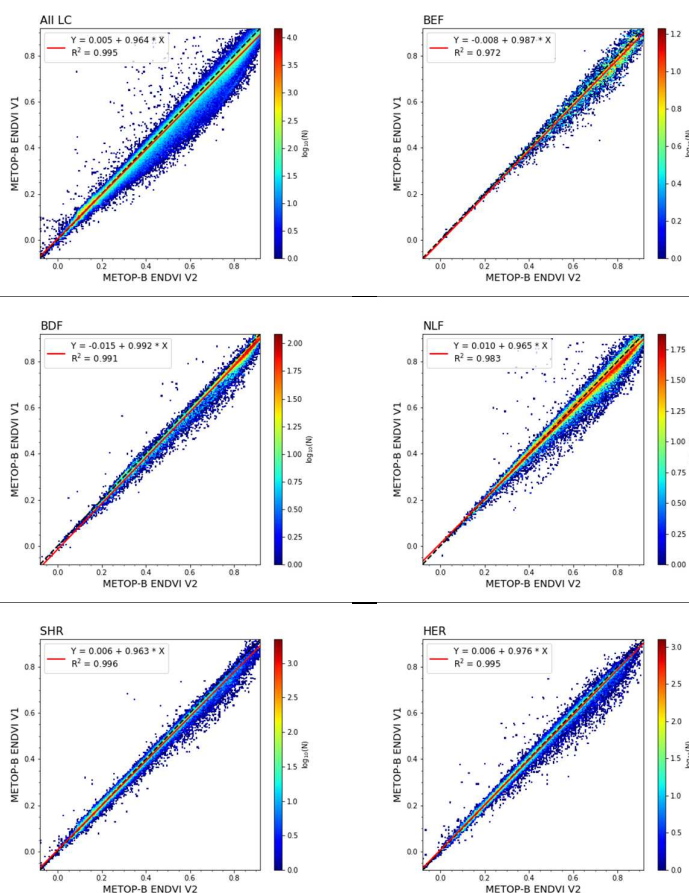


Figure 19. Scatterplots between ENDVI10 v2 (X) and ENDVI10 v1 (Y) over all land cover types (top left) and per biome at global scale, using the 'IllumAngle' sampling scheme.



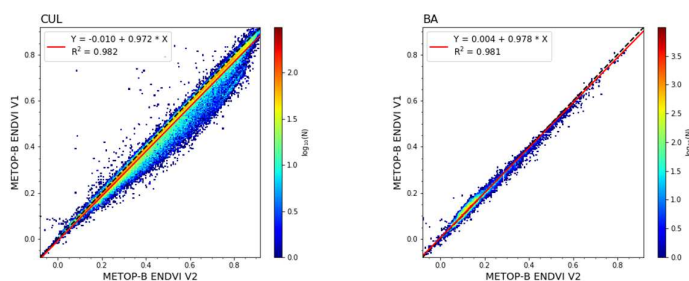
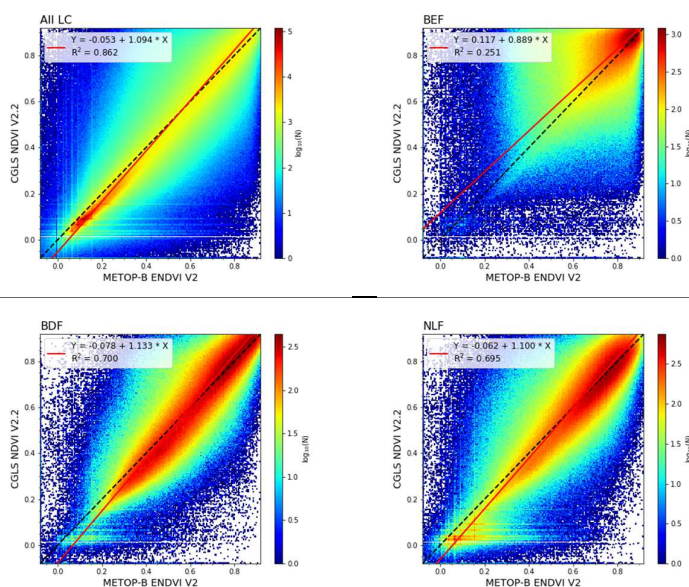


Figure 20. Scatterplots between ENDVI10 v2 (X) and ENDVI10 v1 (Y) over all land cover types (top left) and per biome at global scale, using the 'ViewAngle+IllumAngle' sampling scheme.

3.3.2 Comparison with CGLS NDVI v2.2

Comparisons between ENDVI10 v2 against CGLS NDVI v2.2 are shown in Figure 21. The aggregated results (upper left panel) indicate a generally good agreement, with $R^2=0.86$ and regression slope and intercept values of 1.09 and -0.05, respectively. The coefficient of determination is thus within the product requirement threshold accuracy level. The large scatter mainly results from differences in viewing and illumination angles between observations selected in ENDVI10 v2 and CGLS NDVI v2.2, which are both 10-daily maximum NDVI value composites, differences in spectral response (see Annex 1), differences in AOT used in the atmospheric correction, different cloud, cloud shadow and snow masking performances, and differences in absolute radiometric calibration. The aggregated results show that in general the NDVI values < 0.4 in ENDVI10 v2 are slightly higher compared to CGLS NDVI v2.2. For higher NDVI, the differences tend to be less prominent.



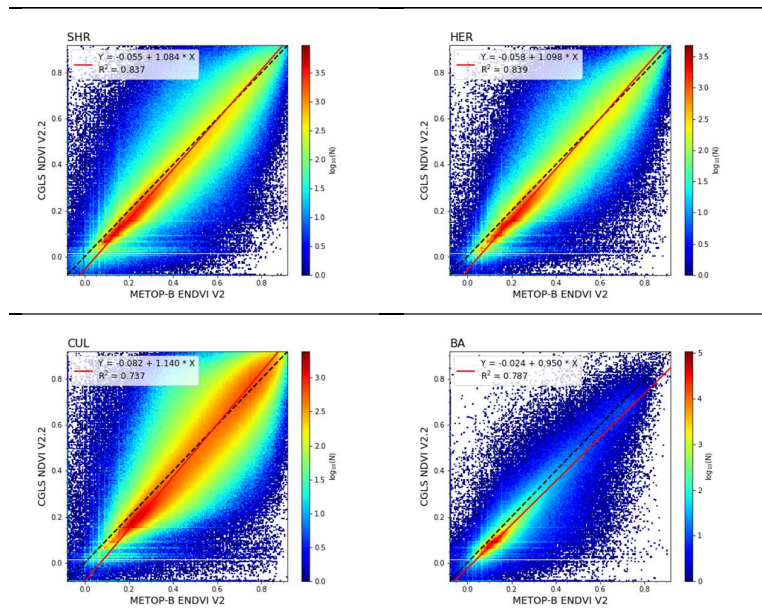
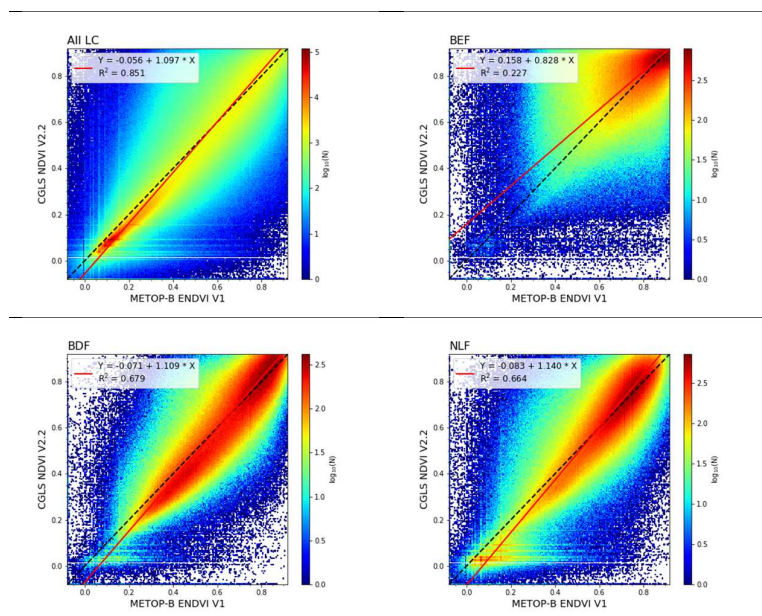


Figure 21. Scatterplots between ENDVI10 v2 (X) and CGLS NDVI v2.2 (Y) over all land cover types (top left) and per biome at global scale.

Scatterplots for aggregated results and per biome for ENDVI10 v1 vs CGLS NDVI v2.2 are presented in Figure 22. When comparing the scatterplots of Figure 21 and Figure 22, the results are nearly identical for all biomes. This demonstrates, as already seen in §3.3.1, that ENDVI10 v2 and v1 are statistically very consistent.



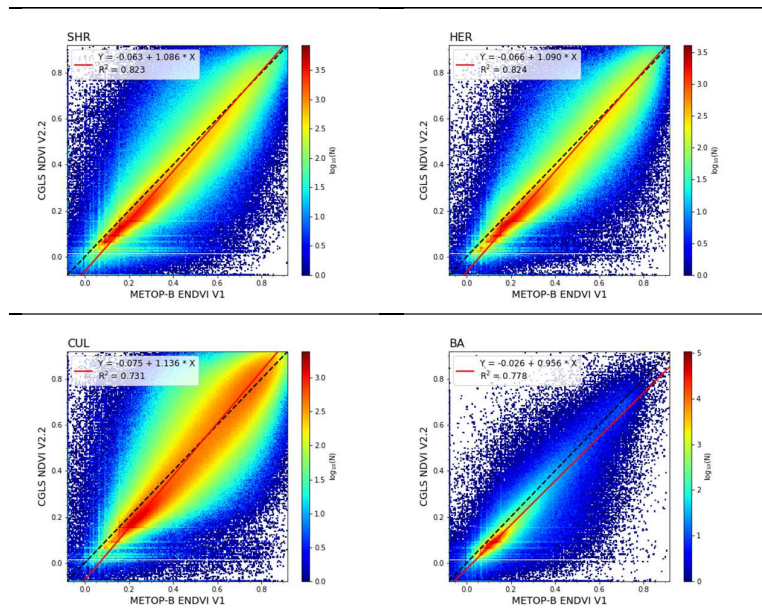


Figure 22. Scatterplots between ENDVI10 v1 (X) and CGLS NDVI v2.2 (Y) over all land cover types (top left) and per biome at global scale.

3.4 Temporal consistency

3.4.1 Temporal smoothness

The δ parameter (Vermote et al., 2009) expresses the temporal smoothness of the NDVI profiles (see also Table 2). Figure 23 shows the intercomparison of δ frequency histograms for ENDVI10 v2, ENDVI10 v1 and CGLS NDVI v2.2. ENDVI10 v2 is slightly less smooth than ENDVI10 v1, and less smooth than CGLS NDVI v2.2, as indicated by a lower frequency of the lowest δ values.

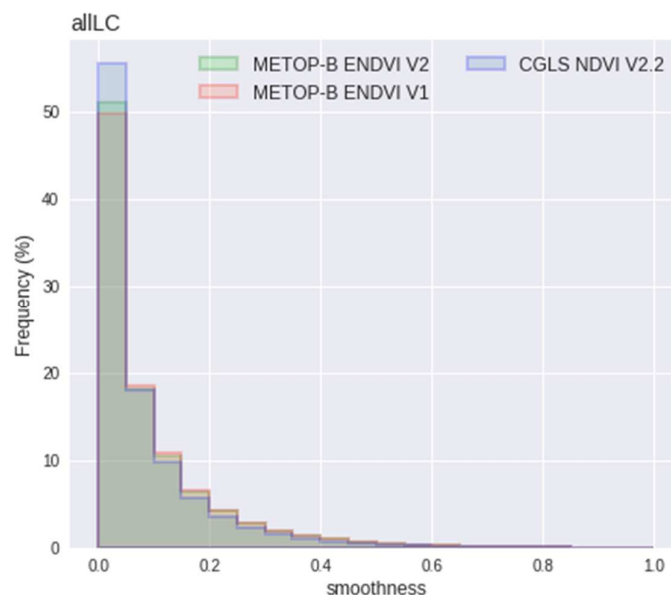


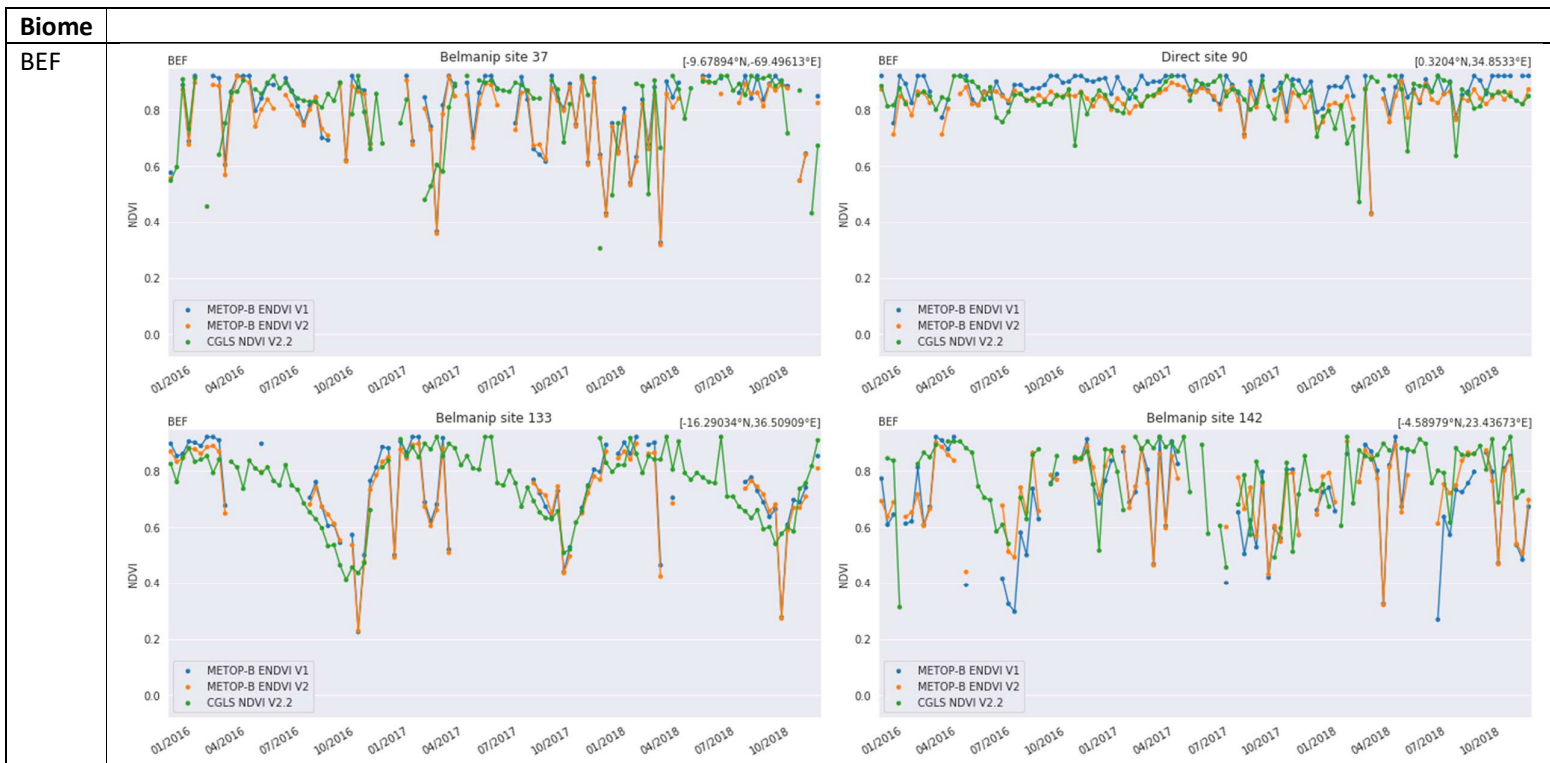
Figure 23. Intercomparison of δ frequency histograms , a measure for temporal smoothness.

3.4.2 Temporal variations and realism

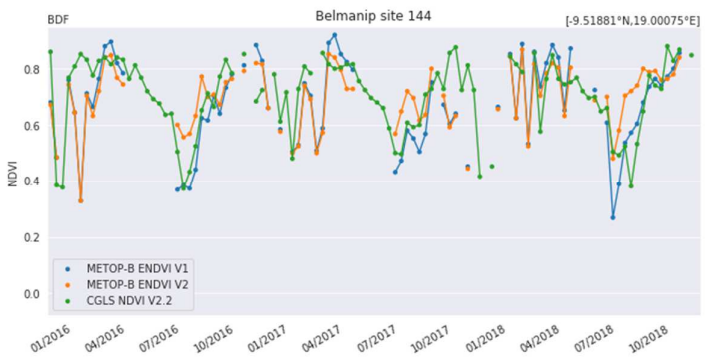
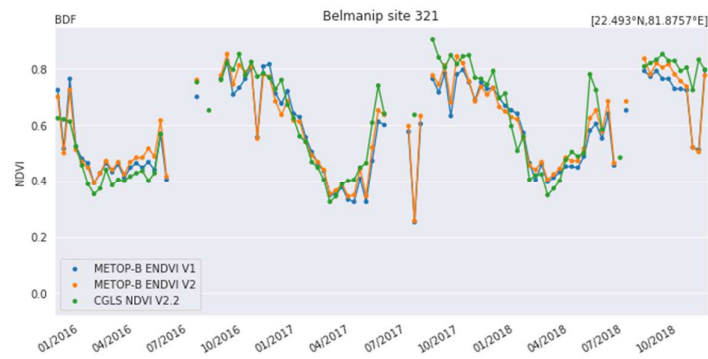
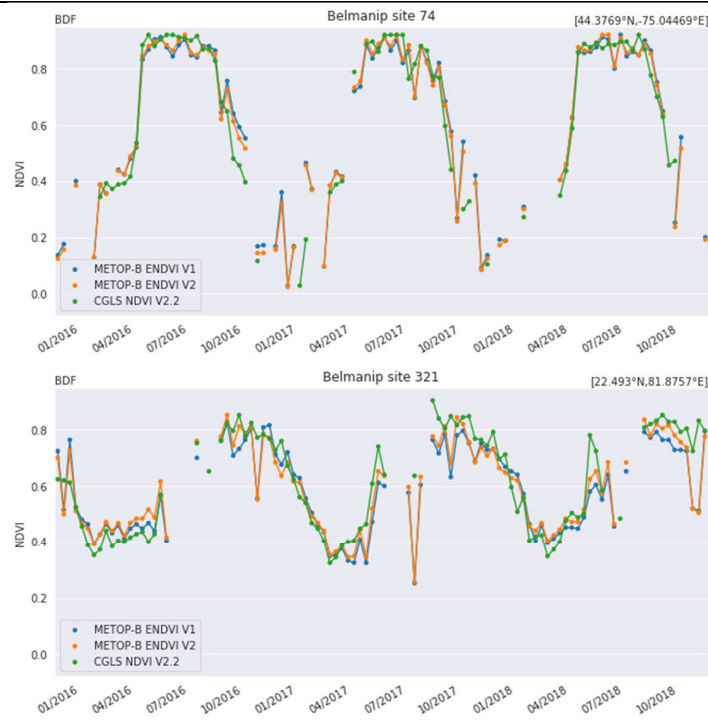
Temporal pixel profiles were extracted over the BELMANIP2/Direct sites. Figure 24 shows various examples with a comparison of the temporal profiles of ENDVI10 v2 (orange), ENDVI10 v1 (blue) and CGLS NDVI v2.2 (green).

The profiles in Figure 24 generally show good agreement between ENDVI10 v2 and ENDVI10 v1, although for some sites deviations occur. For example, over Direct site 90 (W Kenya) the ENDVI10 v2 values are more in line with CGLS NDVI v2.2, while the ENDVI10 v1 values often saturate and are significantly higher. Drops in the profile, possibly due to undetected clouds or snow, occur both in ENDVI10 v2 and in ENDVI10 v1 (e.g. BEF Belmanip 37 (Mongolia), Belmanip 133 (Mozambique); BDF Belmanip 159 (E Central African Republic), Belmanip 321 (India), Belmanip 144 (Angola); NLF Belmanip 325 (E China); HER Belmanip 58 (S USA)). A number of profiles however show less temporal noise in ENDVI10 v2 compared to ENDVI10 v1 (BEF Belmanip site 142 (DR Congo); NLF Direct 5 (NW USA); SHR Direct 61 (Morocco)). Also the profiles over BA are more stable in ENDVI10 v2 compared to ENDVI10 v1. Over BA sites, CGLS NDVI v2.2 has considerably lower NDVI. This can be attributed to the difference in absolute calibration and the different SRFs of the sensors (see Annex 1).

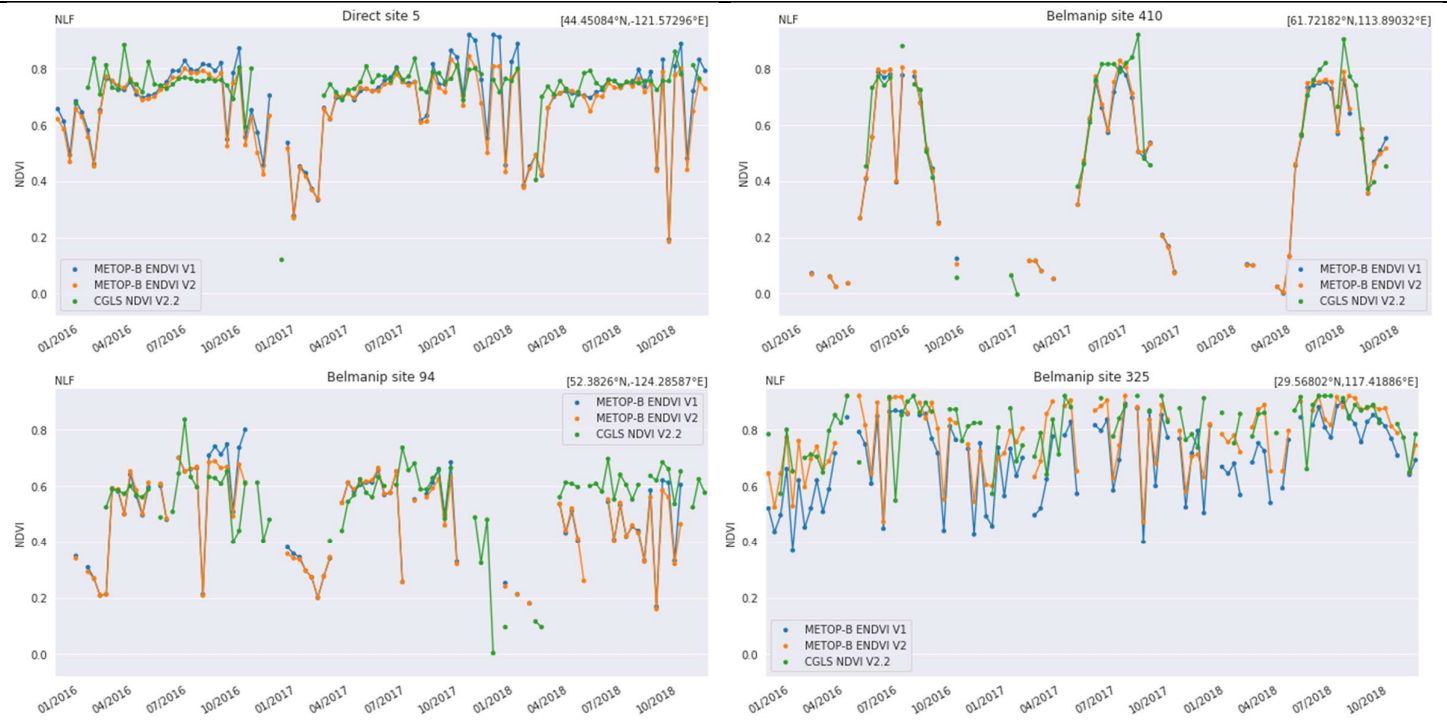
For a very limited number of sites, the differences between MetOp-B ENDV v2 and ENDVI10 v1 are relatively large. In Annex 3 these cases are investigated in detail. These sites are all located in Asia, where the difference between the AOT used in ENDVI10 v2 vs the AOT used in ENDVI10 v1 is the largest.

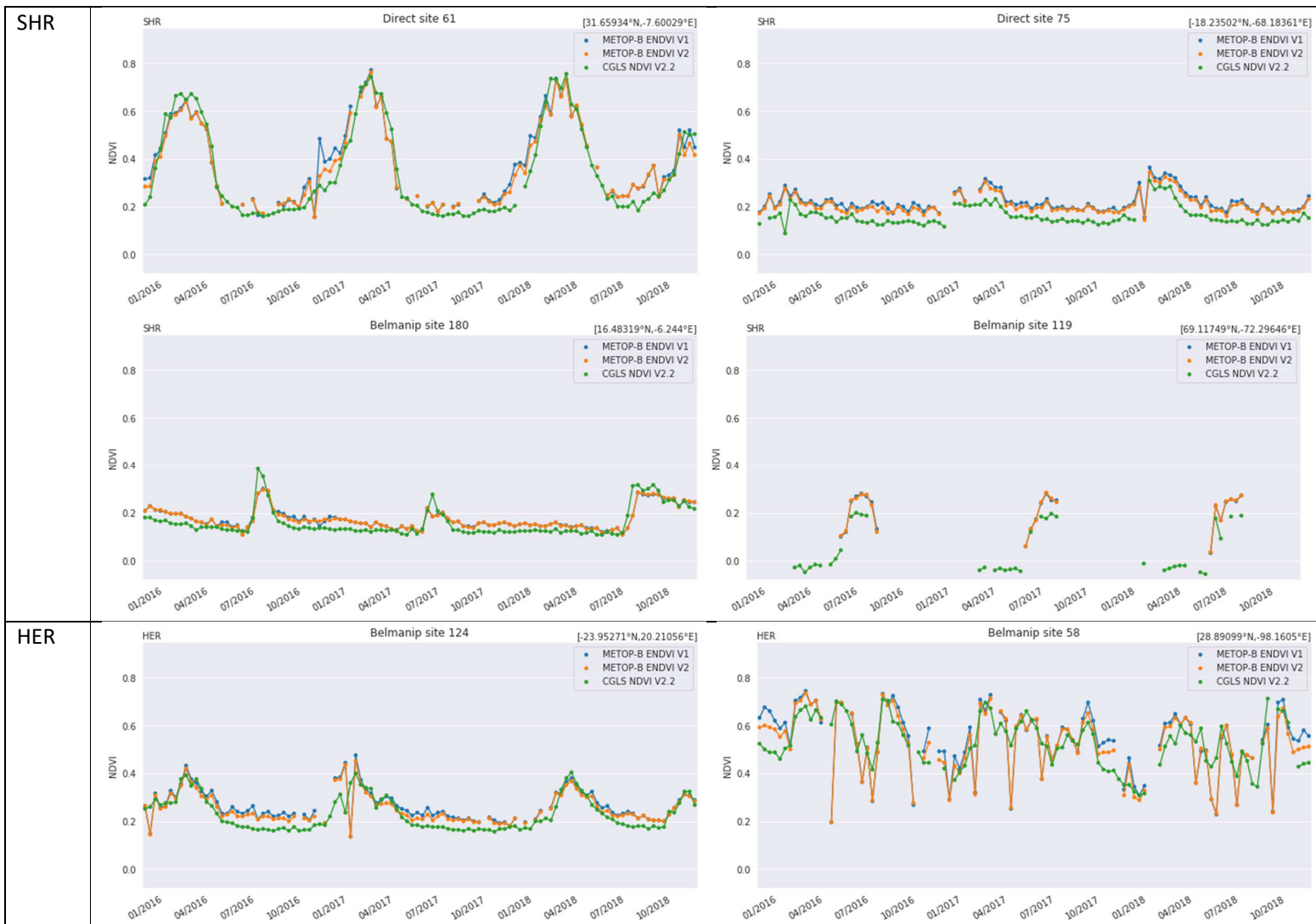


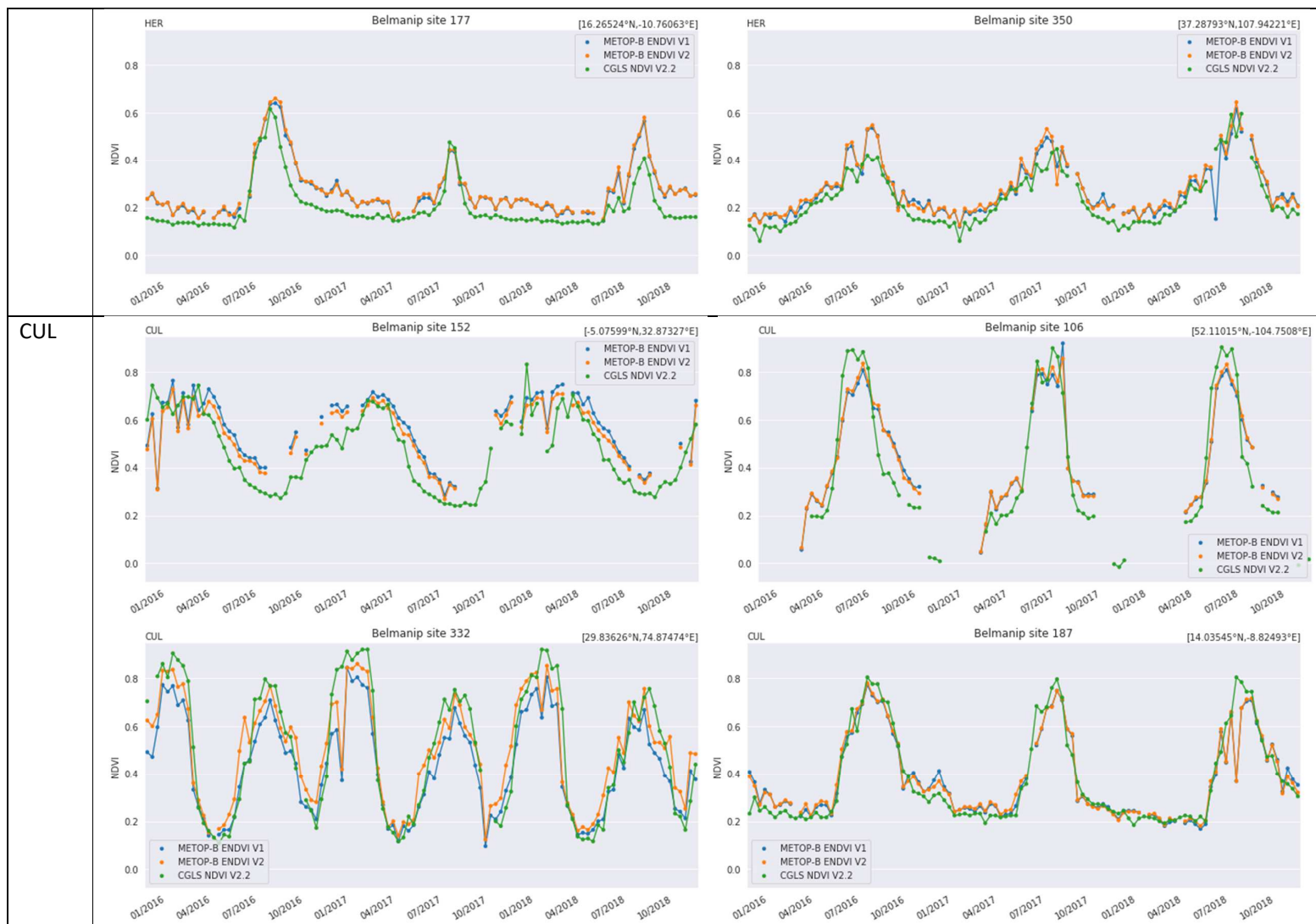
BDF



NLF







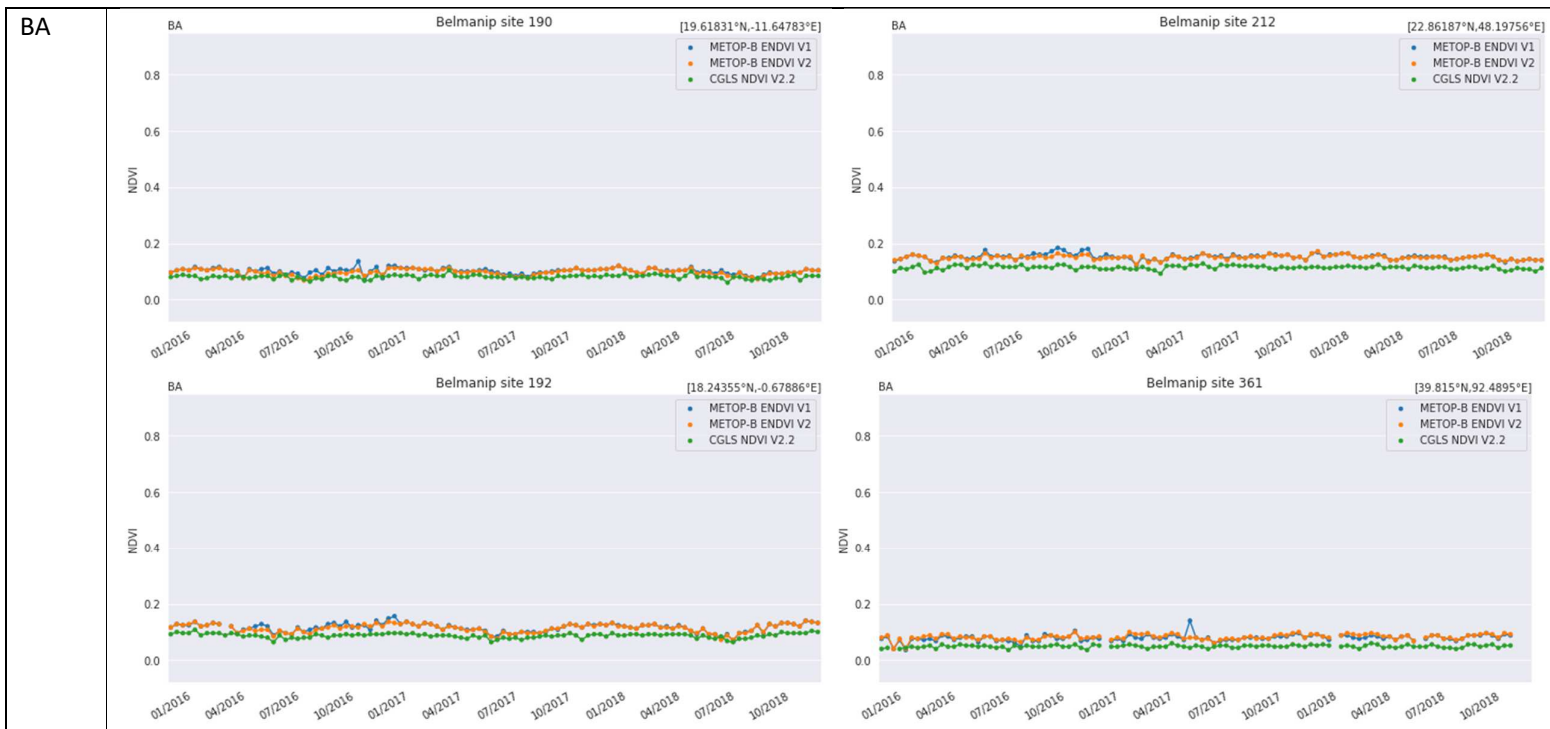


Figure 24. Temporal profiles of ENDVI10 v2, ENDVI10 v1 and CGLS NDVI V2.2 over a number of BELMANIP2 and DIRECT sites

4 Consistency between sensors

4.1 Radiometry (ENDVI10)

4.1.1 MetOp-A vs. MetOp-B (2016)

The radiometric consistency between MetOp-A and MetOp-B is evaluated through Intercomparison of ENDVI10 v2 over the period January – December 2016. Since April 2013, MetOp-A has been acting as the back-up for MetOp-B. However, the MetOp-A active orbit has been suspended from June 2017 onwards. Therefore for this analysis, ENDVI10 v2 was generated over the period with orbit-controlled MetOp-A input.

As the orbits of MetOp-A and -B are the same, but shifted by 48.93 minutes, a representative sample of the separate biomes could not be obtained (see §2.3). Therefore, only the results of all land cover classes are shown here. There is a large agreement between the NDVI of MetOp-A and -B (Figure 25), although the NDVI of MetOp-A is slightly higher than that of MetOp-B. This is in line with what was observed in the past, when the consistency between ENDVI10 v1 was evaluated between MetOp-A and -B (Swinnen and Dierckx, 2015).

Although MetOp-A and -B have the same equator crossing time, due to the shift in their orbit an observation of the same location on Earth is acquired at a different local time, because it is positioned elsewhere across-track. Figure 27 shows the histograms of the VZA of paired observations without additional sampling and with the ‘ViewAngle’ condition applied. In both cases, there is a significant difference in the VZA, with lower VZA for MetOp-B compared to MetOp-A. The (small) systematic difference observed in Figure 25 could therefore be attributed to directional effects.

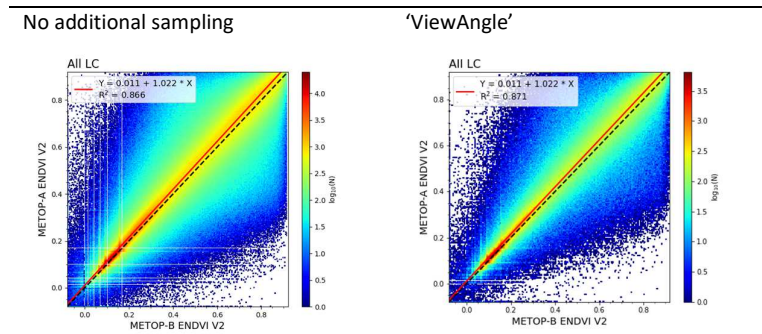


Figure 25. Scatterplots between MetOp-B ENDVI10 v2 (X) and MetOp-A ENDVI10 v2 (Y) over all biome types. Analysis without additional sampling (left) and with additional ‘ViewAngle’ sampling (right).

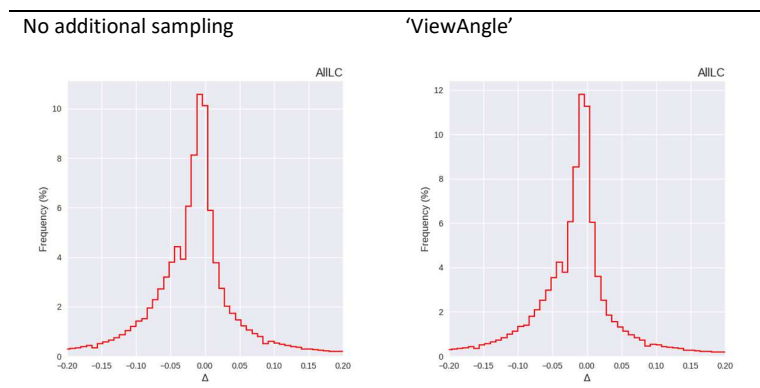


Figure 26. Histograms of the bias between MetOp-B ENDVI10 v2 and MetOp-A ENDVI10 v2 over all land cover types. Analysis without additional sampling (left) and with additional ‘ViewAngle’ sampling (right).

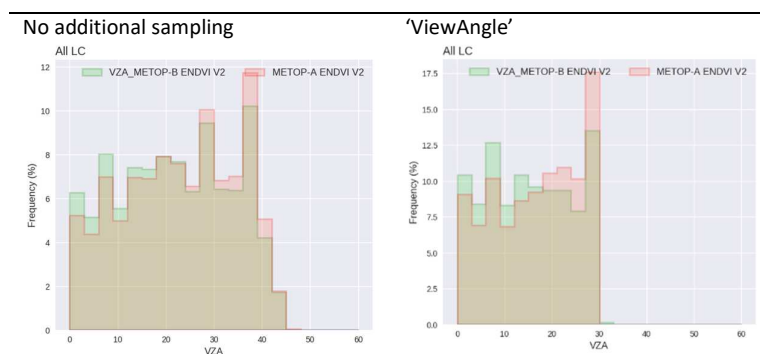


Figure 27. Histograms of the VZA of paired observations between MetOp-B ENDVI10 v2 and MetOp-A ENDVI10 v2 over all land cover types. Analysis without additional sampling (left) and with additional ‘ViewAngle’ sampling (right).

4.1.2 MetOp-B vs. MetOp-C (2019)

The radiometric consistency between MetOp-B and MetOp-C is evaluated through intercomparison of ENDVI10 v2 over the period July 2019 – September 2019. Both satellites are configured in a phasing of 120 degrees (Borde et al., 2019). Because MetOp-C is in operations from 3 July 2019 and some input data of the last dekad of September 2019 were missing, the product completeness of MetOp-C is slightly lower in the first and last dekad of this period. Nevertheless, as the overlap period between both sensors is short, we opted to include all available dekads, to have as much paired observations as possible for the statistical analysis. As for the previous analysis, the results are only shown for all land cover types.

Figure 28 shows the scatterplots between MetOp-B and -C, while Figure 29 presents the bias histograms. Both show that the ENDVI10 v2 from both sensors are very similar. Further, the bias histograms are more narrow than the ones between MetOp-A and -B. The histograms of the VZA (Figure 30) show a less clear distinction between the VZA compared to Figure 27, which indicates directional effects might play a smaller role in this intercomparison.

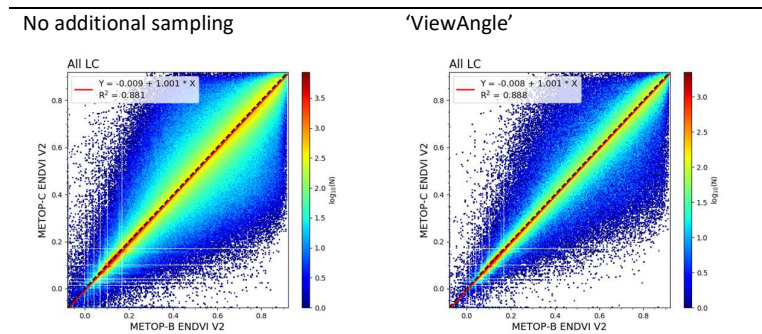


Figure 28. Scatterplots between MetOp-B ENDVI10 v2 (X) and MetOp-C ENDVI10 v2 (Y) over all biome types. Analysis without additional sampling (left) and with additional 'ViewAngle' sampling (right).

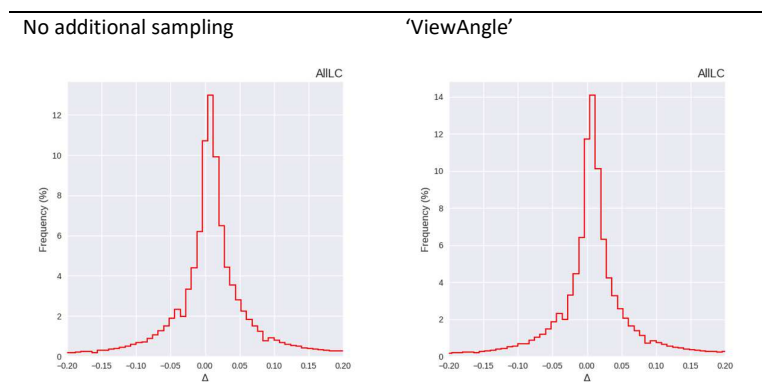


Figure 29. Histograms of the bias between MetOp-B ENDVI10 v2 (X) and MetOp-C ENDVI10 v2 (Y) over all land cover types. Analysis without additional sampling (top left) and with additional 'ViewAngle' sampling (right).

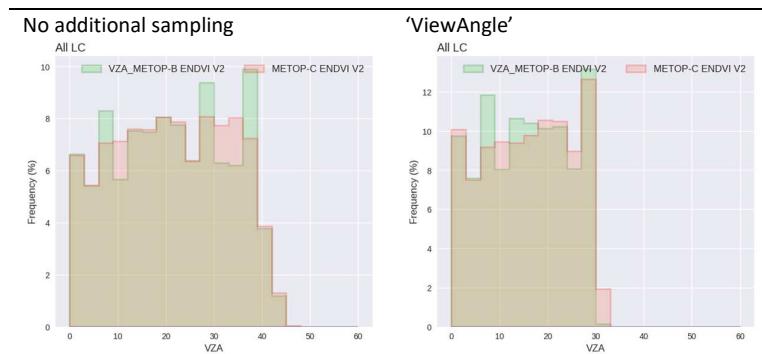


Figure 30. Histograms of the VZA of paired observations between MetOp-B ENDVI10 v2 and MetOp-A ENDVI10 v2 over all land cover types. Analysis without additional sampling (left) and with additional 'ViewAngle' sampling (right).

4.1.3 MetOp-A, -B, -C vs. CGLS NDVI v2.2

In order to evaluate the spatio-temporal consistency between MetOp-A, -B and -C, a test ENDVI10 v2 dataset was created based on the combination of three sensors. The test dataset is

based on MetOp-A input from January – December 2016, on MetOp-B input from January 2017 – June 2019, and on MetOp-C from July 2019 – September 2019. This combined dataset is intercompared with CGLS NDVI v2.2, which is based on a single sensor (PROBA-V) for this period.

Figure 31 shows the RMSD, also split into systematic (RMPDs) and unsystematic (RMPDu) differences, as well as the overall mean bias error (MBE). The magnitude of the metrics are in line with the previously discussed results (see mainly Figure 14 and Figure 16). There is a latitudinal dependence of the difference between ENDVI10 v2 and CGLS NDVI v2.2, which is related mainly with changes in major biomes. The differences are largest over the equatorial area, with as dominant landcover EBF, for which the CGLS NDVI v2.2 is higher. The Sahara is the most dominant area in the latitude band around 20°N. Here, the differences are the smallest, and have an opposite sign. For the other biomes, there is a larger range in NDVI values. We also observe a seasonal change in these differences.

The most important result of this analysis is that the seasonal variation of the differences exhibit a stable pattern over the years. The sensor changes between MetOp-A, -B, and -C cannot be identified in this Hovmöller plots. This implies that the ENDVI10 v2 provides a consistent time series over the different sensors.

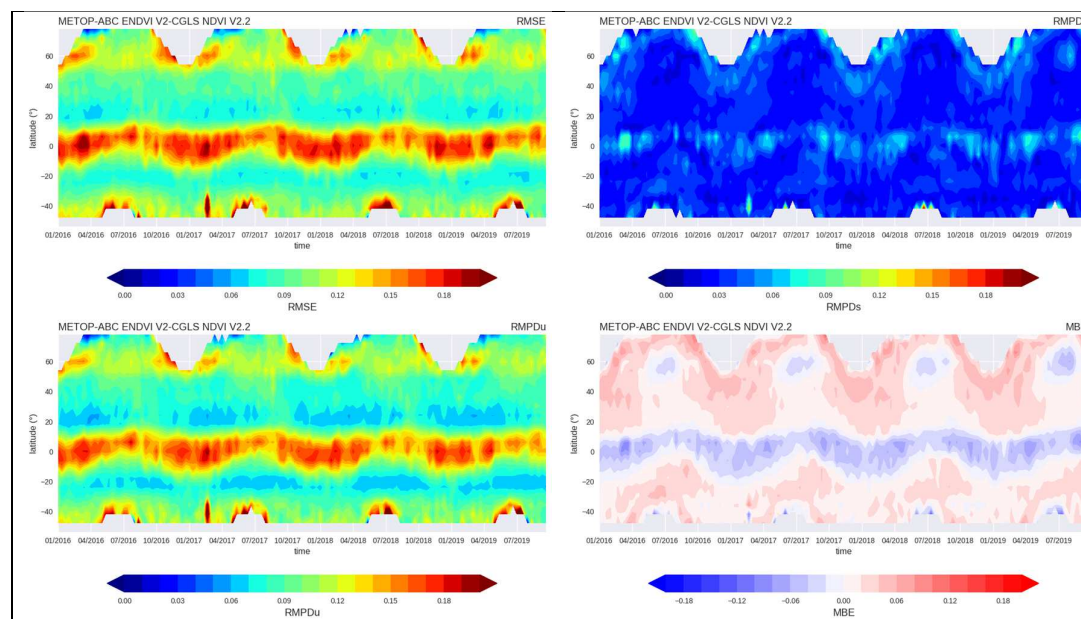
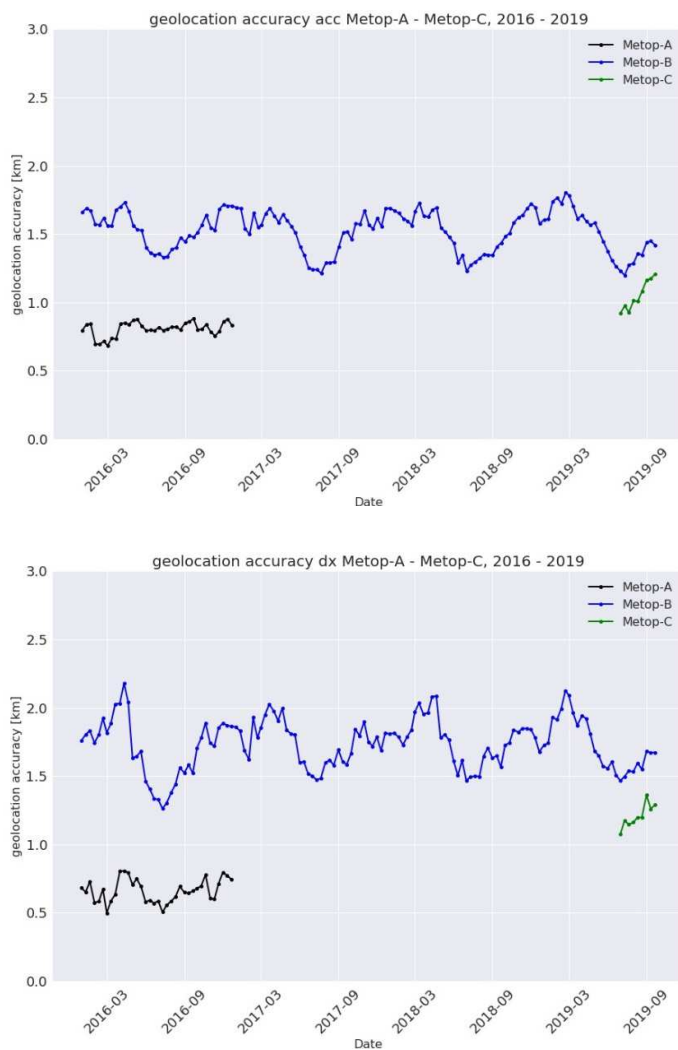


Figure 31. Hovmöller plots showing the spatio-temporal distribution of RMSD, RMPDs, RMPDu and MBE between a test dataset of ENDVI10 v2 combining MetOp-A, -B, and -C with CGLS NDVI v2.2 for January 2016 – September 2019.

4.2 Geometric accuracy

A measure for the geolocation accuracy is obtained by comparing the S10 pixels' geolocation to a large amount of globally distributed Ground Control Points (GCPs, see §2.4). Time series plots of the mean geolocation accuracy (i.e., the mean deviation from the geolocation GCP reference geolocation) are shown in Figure 32 for the aggregated latitudinal (dx) and longitudinal

(dy) deviations (upper panel), as well as for the separate dx and dy components (middle and bottom panel, respectively).



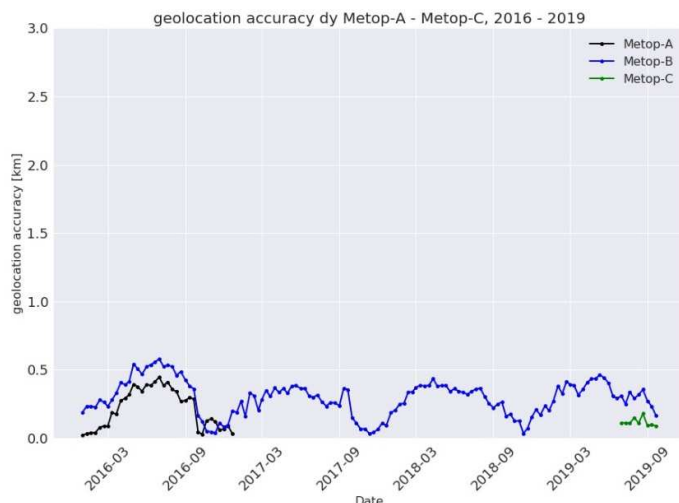


Figure 32. Geolocation accuracy for MetOp-A – C, 2016 – 2019, for (upper panel) aggregated longitudinal (dx) and latitudinal (dy) deviations, (middle panel) dx deviations, and (bottom panel) dy deviations.

The time series reveal that MetOp-A has a more accurate geolocation (lower mean deviations of ~ 0.8 km) compared MetOp-B, at least for 2016, the year for which ENDVI10 v2 was generated for both platforms. Further, for the limited data available over 2019 (July through September), MetOp-B exhibits geometric deviations that are ~ 0.3 km larger than for MetOp-C. Finally, the MetOp-B geolocation accuracy exhibits a seasonal cycle, with maxima (i.e., less accurate geolocation) during the boreal winter months, and minima (better geolocation accuracy) during the boreal summer months. The geolocation accuracy for MetOp-A appears to be more stable and shows this seasonal pattern to a much lesser extent, at least for the dx component in the single year investigated.

For all platforms, the geolocation accuracy for dy is considerably better than for dx , with only small differences (~ 0.3 km or less) between MetOp-B and -A for 2016 and MetOp-B and -C for July – September 2019. The difference between the dx and dy geolocation accuracy is most pronounced for MetOp-B, with differences dy vs dx between ~ 0.7 – 1.5 km. A remarkable feature is that the seasonal cycles for MetOp-B dx and dy are out of phase.

The large difference in dx and dy geolocation for MetOp-B has been addressed in a recent discussion paper of Wu et al. (2019, in review) on AVHRR GAC geolocation accuracy for NOAA-17, MetOp-A, and -B. The paper demonstrates an inferior across-track (i.e. dx) geolocation for MetOp-B in case of large VZA combined with topographic effects, with the error increasing for increasing VZA. Although the analysis was done on AVHRR GAC data, in which the nominal AVHRR data are subsampled in the along-track and averaged and subsampled in the across-track direction, we suspect the observed inferior MetOp-B dx geolocation being likely due to the AVHRR input data for the following reasons: first, the processing chain has been scrutinized to ascertain that no different geometric processing is done for MetOp-B compared to MetOp-A and -C, which was confirmed. Second, as the AVHRR GAC data processing averages pixels in the across-track direction, any random deviations in this direction would largely cancel out, while any any systematic dx deviations will still be visible. Finally, the reported large geolocation dx deviations over high terrain and for large VZA is supported by spatial dx deviation plots from the

chipmatching output. Figure 33 exemplifies the difference in MetOp-A vs -B geolocation accuracy for the aggregated accuracy and the separate dx and dy components for 20160401.

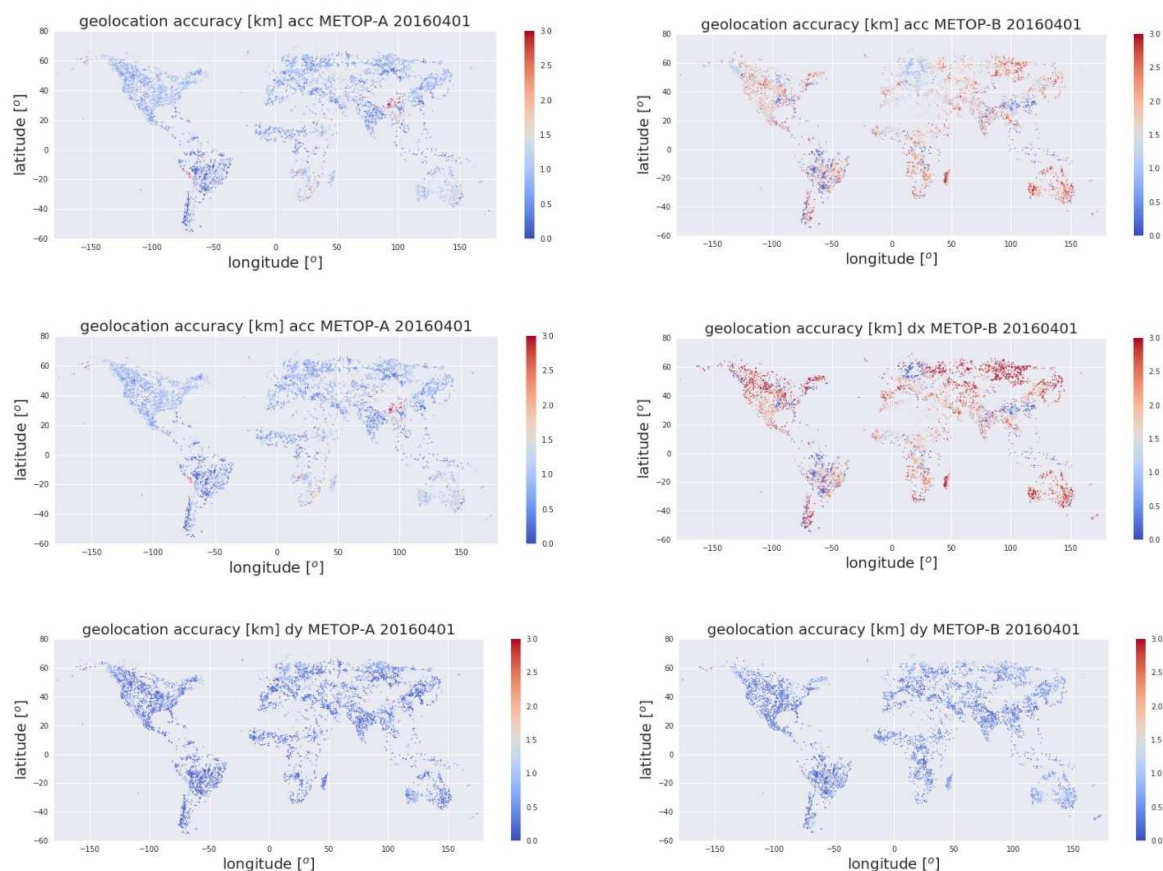


Figure 33. Geolocation S10 accuracy values for 20160401 for MetOp-A (left column) and MetOp-B (right column). The upper row shows the aggregated dx and dy geolocation accuracy, while the separate dx and dy components (expressed in absolute values) are shown in the middle and bottom row, respectively. Low geolocation deviations are indicated by blue colors and transform towards red for larger deviations.

5 Summary and conclusions

This VR focused on product completeness, spatial, statistical, and temporal consistency of the ENDVI10 v2 (LSA-420 and LSA-454), by comparing data over 2016 - 2018 with the previous ENDVI10 v1 and an external NDVI reference dataset from CGLS NDVI v2.2. The main findings are summarized here:

- **Product completeness**

ENDVI10 v2 shows very similar product completeness to ENDVI10 v1 in terms of temporal evolution, spatial distribution, and gap length frequency. The average amount of good observations is 71%, with the largest occurrence of gaps in the Northern Hemisphere winter months and at higher latitudes.

- **Spatial consistency**

Compared to ENDVI10 v1, over dense forests, ENDVI10 v2 shows slightly lower frequencies of the highest NDVI ranges. There is a slight shift towards lower NDVI values for biomes with lower NDVI values. Systematic differences are most pronounced over areas where the difference between CAMS_{CLIM} AOT and the static latitudinal function are largest. Differences with CGLS NDVI v2.2 are resulting from a complex combination of differences in sensor characteristics, absolute calibration, processing choices, and directional effects that are difficult to separate.

- **Statistical consistency**

ENDVI10 v2 and ENDVI10 v1 show very high statistical consistency, with slightly lower frequencies of high ENDVI10 v2 compared to ENDVI10 v1 over densely forested areas and a slight skewedness towards higher ENDVI10 v2, which is related to differences in the AOT input between ENDVI10 v1 and ENDVI10 v2.

- **Temporal consistency**

Temporal profiles over BELMANIP2/Direct sites generally show very good agreement between ENDVI10 v2 and ENDVI10 v1. ENDVI10 v2 shows a slightly lower temporal smoothness than ENDVI10 v1.

In addition, the consistency between the MetOp-A, -B and -C sensors was investigated. To evaluate the radiometric consistency between MetOp-A, -B and -C, statistical consistency was analyzed between ENDVI10 v2 derived from MetOp-A and -B over January – December 2016, and between ENDVI10 v2 derived from MetOp-B and -C over the period July – September 2019. The geometric accuracy was evaluated based on the comparison of the geolocation the ENDVI10 v2 to a number of globally distributed Ground Control Points (CGPs).

- **Radiometric consistency**

ENDVI10 v2 shows large agreement between MetOp-A and -B, and MetOp-B and -C. The ENDVI10 v2 of MetOp-A is slightly higher than that of MetOp-B, which is in line with what was observed for ENDVI10 v1 in the past (Swinnen and Dierckx, 2015). The bias between MetOp-B and -C ENDVI10 v2 is smaller. Seasonal variation of the differences between a

combined ENDVI10 v2 dataset based on MetOp-A/B/C and CGLS NDVI v2.2 over 2016 – 2019 shows a stable pattern over the years. ENDVI10 v2 thus provides **a consistent time series over the different sensors**.

- **Geometric accuracy**

Time series analysis of geolocation accuracy shows that MetOp-A and -C have a more accurate geolocation compared to MetOp-B, which is in agreement with findings of Wu et al. (2019, in review). For all three platforms, latitudinal geolocation is considerably better than longitudinal geolocation.

In conclusion, based on the findings of the validation of ENDVI10 v2 and the consistency analysis between sensors, **ENDVI10 v2 is of sufficiently good quality to be operationally distributed to the users**. Differences between ENDVI10 v2 and ENDVI10 v1 are very small, and can be attributed to the different AOT input (CAMS_{CLIM} vs. static AOT) used in the atmospheric correction. The temporal profiles over BELMANIP2/DIRECT sites show slightly improved consistency of ENDVI10 v2 with CGLS NDVI v2.2, in comparison to ENDVI10 v1, although from the statistical consistency analysis these differences appear to be not significant.

References

- Baret, F., Morisette, J.T., Fernandes, R. a., Champeaux, J.L., Myneni, R.B., Chen, J., Plummer, S., Weiss, M., Bacour, C., Garrigues, S., Nickeson, J.E., 2006. Evaluation of the representativeness of networks of sites for the global validation and intercomparison of land biophysical products: Proposition of the CEOS-BELMANIP. *IEEE Trans. Geosci. Remote Sens.* 44, 1794–1802. <https://doi.org/10.1109/TGRS.2006.876030>
- Bartholomé, E., Belward, A.S., 2005. GLC2000: a new approach to global land cover mapping from Earth observation data. *Int. J. Remote Sens.* 26, 1959–1977. <https://doi.org/10.1080/01431160412331291297>
- Borde, R., Carranza, M., Hautecoeur, O., Barbieux, K., 2019. Winds of Change for Future Operational AMV at EUMETSAT. *Remote Sens.* 11, 2111. <https://doi.org/10.3390/rs11182111>
- Duveiller, G., Fasbender, D., Meroni, M., 2016a. Supplementary information for: Revisiting the concept of a symmetric index of agreement for continuous datasets. *Sci. Rep.* 6, 19401. <https://doi.org/10.1038/srep19401>
- Duveiller, G., Fasbender, D., Meroni, M., 2016b. Revisiting the concept of a symmetric index of agreement for continuous datasets. *Sci. Rep.* 6, 1–14. <https://doi.org/10.1038/srep19401>
- Garrigues, S., Lacaze, R., Baret, F., Morisette, J.T., Weiss, M., Nickeson, J.E., Fernandes, R., Plummer, S., Shabanov, N. V., Myneni, R.B., Knyazikhin, Y., Yang, W., 2008. Validation and intercomparison of global Leaf Area Index products derived from remote sensing data. *J. Geophys. Res. Biogeosciences* 113. <https://doi.org/10.1029/2007JG000635>
- Inness, A., Ades, M., Agustí-Panareda, A., Barré, J., Benedictow, A., Blechschmidt, A., Dominguez, J.J., Engelen, R., Eskes, H., Flemming, J., Huijnen, V., Jones, L., Kipling, Z., Massart, S., Parrington, M., Peuch, V., Razinger, M., Remy, S., Schulz, M., Suttie, M., 2019. The CAMS reanalysis of atmospheric composition. *Atmos. Chem. Phys.* 19, 3515–3556. <https://doi.org/10.5194/acp-19-3515-2019>
- NASA, 2014. CEOS LPV guidelines [WWW Document]. URL https://lpvs.gsfc.nasa.gov/LPV_CS_gen.html
- Rahman, H., Dedieu, G., 1994. SMAC: a simplified method for the atmospheric correction of satellite measurements in the solar spectrum. *Int. J. Remote Sens.* 15, 123–143. <https://doi.org/10.1080/01431169408954055>
- Swinnen, E., Dierckx, W., 2015. Validation Report - Normalized Difference Vegetation Index. SAF/LAND/VITO/VR_endvi/2.0.
- Wu, X., Naegeli, K., Wunderle, S., 2019. Geometric accuracy assessment of global coarse resolution satellite data sets: a study based on AVHRR GAC data at the subpixel level. *Earth Syst. Sci. Data Discuss.* In review, 1–22. <https://doi.org/10.5194/essd-2019-87>

Annex 1

PROBA-V, and MetOp/AVHRR Spectral Response Functions and flight characteristics

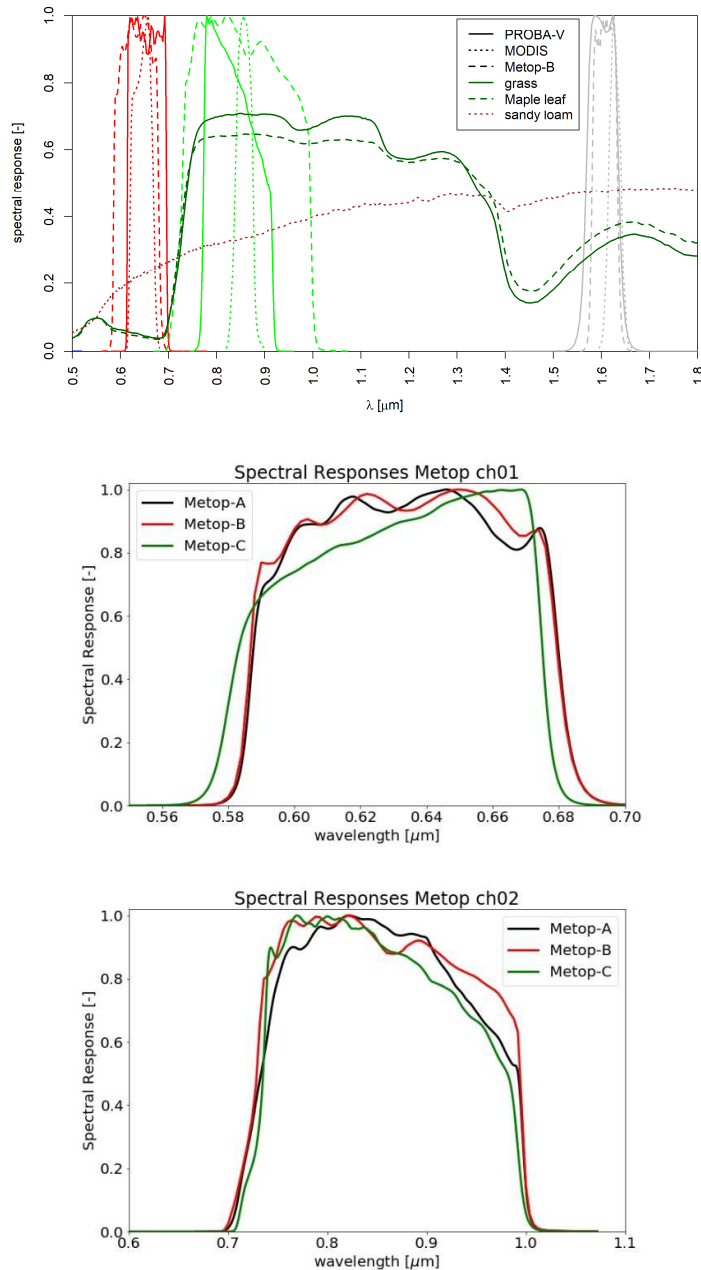


Figure 34. (upper panel) Spectral Response Functions for PROBA-V (solid lines), Terra-MODIS (dotted lines), and MetOp-B-AVHRR (dashed lines). Reference grass, maple leaf, and sandy loam spectra are shown in dark green (solid), dark green (dashed), and dotted brown lines, respectively. (middle panel) RED channel Spectral Response Functions for MetOp-A – C, (bottom panel) NIR channel Spectral Response Functions for MetOp-A – C.

Table 4. PROBA-V and MetOp-B/AVHRR flight characteristics, equatorial overpass times, and RED and NIR spectral ranges (Full Width at Half Maximum, FWHM).

	PROBA-V	MetOp-B/AVHRR
Altitude [km]	820	817
Inclination angle [°]	98.7	98.7
Swath [km]	2250	1447
Equator crossing time (LST) at descending node	10:48 (01/2016) – 10:06 (12/2018)	8:45 (MetOp-B) 9:30 (MetOp-A,-C)
Stability of the platform	Orbital drift, no on-board propellant	No orbital drift
Spectral range RED @FWHM [μm]	0.614 – 0.696	0.587 – 0.679
Spectral range NIR @FWHM [μm]	0.772 – 0.902	0.730 – 0.994

Annex 2

Comparison of CAMS AOT with static latitudinal function

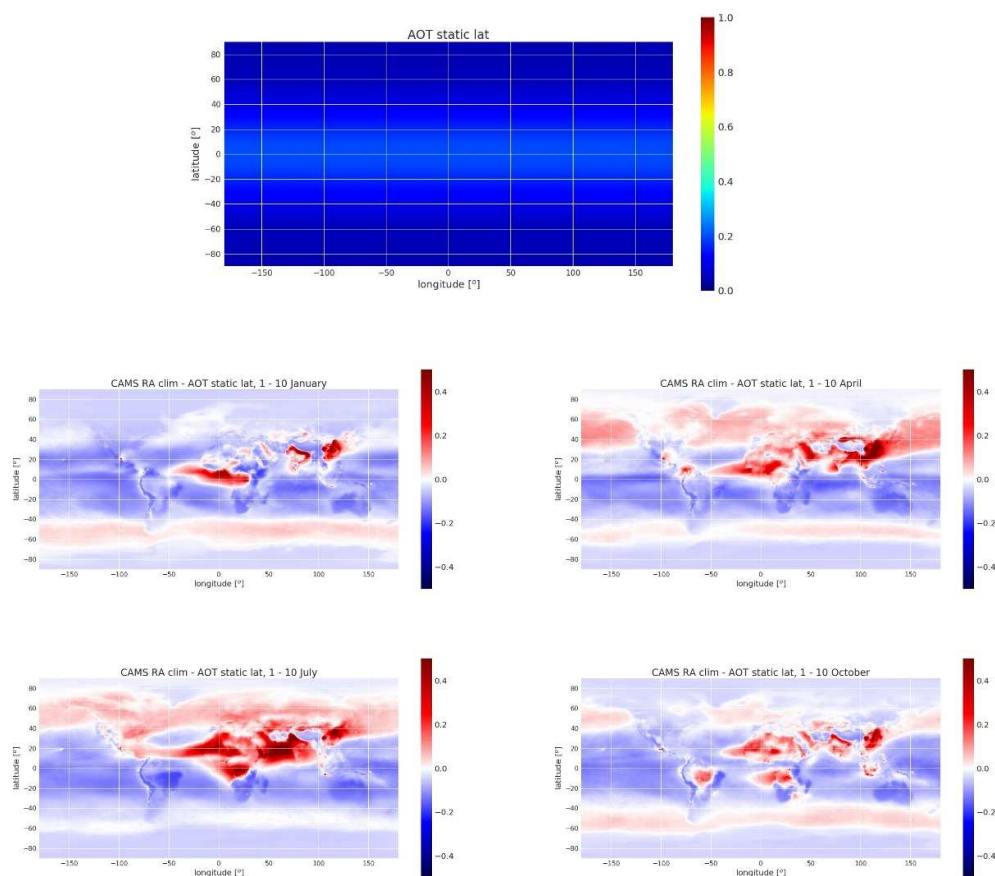
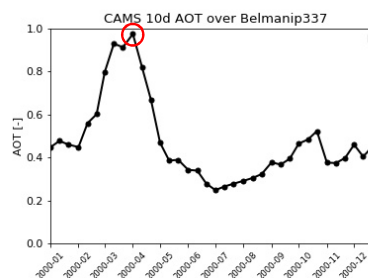
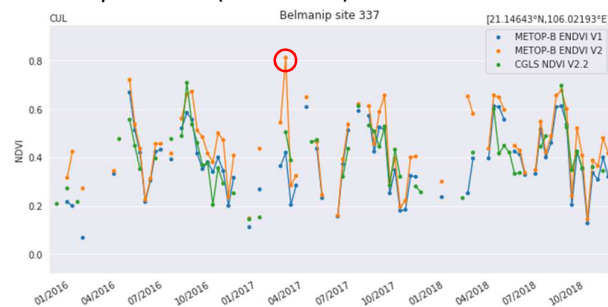


Figure 35. Static latitudinal AOT (upper plot) and the difference between CAMS_{CLIM} and static latitudinal AOT for 1 – 10 January (second row, left), 1 – 10 April (second row, right), 1 – 10 July (bottom row, left), and 1 – 10 October (bottom row, right).

Annex 3

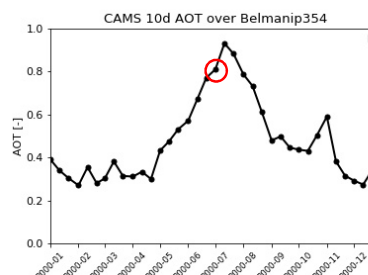
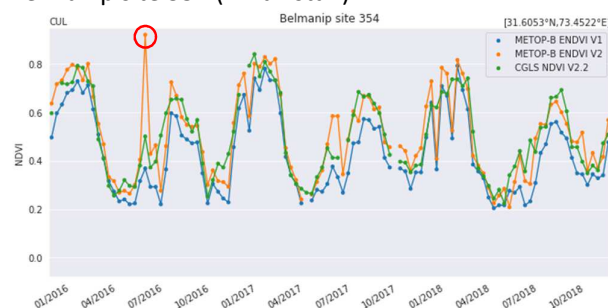
Belmanip sites with larger differences between ENDVI10 v2 and ENDVI10 v1

Belmanip site 337 (N Vietnam)



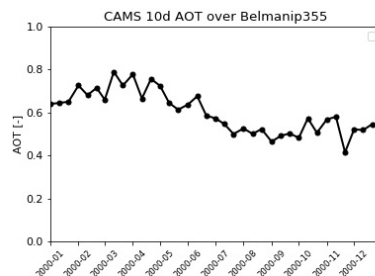
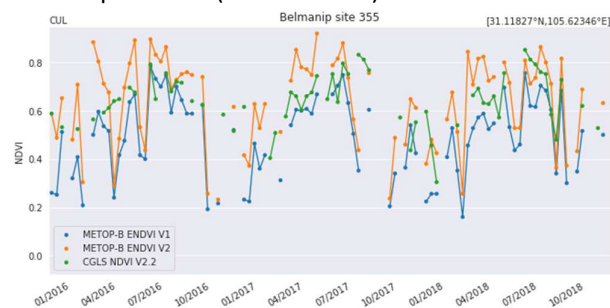
The peak in ENDVI10 v2 at 20170401 is related to a very high AOT of 0.973, in combination with relatively high SZA+VZA ($39^{\circ}+18.5^{\circ}$). The AOT used in ENDVI10 v1 is 0.16. Although the RED_{TOA} is rather high (0.13), the combination of the high AOT used for the AC input and SZA+VZA leads to $RED_{TOC} = 0.015$, which leads to this occasional high NDVI.

Belmanip site 354 (N Pakistan)



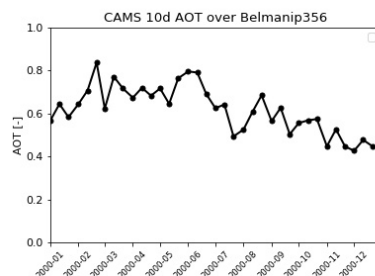
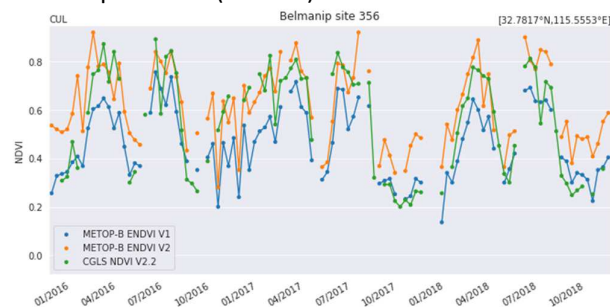
The peak in ENDVI10 v2 at 20160701 is related to a very high AOT of 0.809, in combination with relatively high SZA+VZA ($36^{\circ}+38.5^{\circ}$). The AOT used in ENDVI10 v1 is 0.12. Also in this case, RED_{TOA} is relatively high (0.14), but due to $AOT=0.81$ and the combination of SZA+VZA leads to a sharp NDVI peak of ~ 0.90 . Note that for the same dekade in the other 2 years no sharp NDVI peak is observed.

Belmanip site 355 (central China)



The large difference between the AOT used in ENDVI10 v2 (see graph) and in ENDVI10 v1 (0.13) results in a relatively large difference between ENDVI10 v2 and ENDVI10 v1. For example, at 20170421 the NDVI peaks at 0.88. The RED_{TOA} was 0.10, the AOT used for SMAC was 0.61, which led to a RED_{TOC} of 0.01.

Belmanip site 356 (E China)



Similar to the case above, the large difference between the AOT used in ENDVI10 v2 and in ENDVI10 v1 (0.12) results in a relatively large difference between ENDVI10 v2 and ENDVI10 v1.